REAL-TIME PORTAL IMAGING OF MEGAVOLTAGE THERAPEUTIC PHOTON BEAMS

By

MOHAMMAD KHAIRUL ISLAM

A DISSERTATION PRESENTED TO THE GRADUATE SCHOOL OF THE UNIVERSITY OF FLORIDA
IN PARTIAL FULFILLMENT OF THE REQUIREMENTS FOR THE DEGREE OF DOCTOR OF PHILOSOPHY

UNIVERSITY OF FLORIDA

1987

To my parents
without whose support and sacrifices
my education would not have been possible.

ACKNOWLEDGEMENTS

I would like to express my sincere thanks to the members of my supervisory committee for their invaluable help and guidance throughout this work. My special thanks go to my committee chairman, Dr. Francis Bova, for his help and guidance in all phases of this work. My special thanks are also due to Dr. Lawrence Fitzgerald, my committee co-chairman, for his help and suggestions with my research. I would like to thank Dr. Rodney Million, chairman of the Department of Radiation Therapy, for his interest and support for this project.

My sincere appreciation goes to Dr. Walter Mauderli, who, besides his many helpful suggestions, has spent many laborious hours in helping me with the electronics and instruments design. My special thanks are due to Dr. Genevieve Roessler for her guidance and encouragements throughout my graduate work. Many thanks are due to Dr. Joseph Wilson for his willingness to serve on my committee and for making helpful suggestions.

I would like to give my special thanks to Linda Ewald and Kevin Kalbaugh for their friendship, help, and suggestions throughout this work. They also helped me in preparing the draft of this manuscript. I also express my appreciation to John Priesler for his technical help.

Finally I would like to give special thanks to my wife, Amina, for her patience, understanding, and encouragement during the last phase of my research work.

TABLE OF CONTENTS

		Page
ACKNOWLEDGEMENTS		iii
ABSTRACT		vii
CHAPTERS		
I	INTRODUCTION	1
II	BACKGROUND	4
III	THE FLUORO SYSTEM	9
	System Description	9
	Fluoro-Screen	11
	Metal Screen	13
	Video Camera	20
	Frame Grabber	23
	Image Processing	24
	System Performance and Results	24
	System Efficiency	25
	System Noise	27
	Images	30
	Enhanced Images	35
	Discussion	38
IV	THE CODED APERTURE IMAGING DEVICE	40
	System Description	41
	Radiation Detector	43
	Data Acquisition	65
	Reconstruction and Display	75
	System Performance and Results	76
	System Noise	76
	Spatial Resolution	77
	Contrast Resolution	78
	Images	92
	Enhanced Images	105
	Discussion	106
V	IMAGE PROCESSING	108
	Preprocessing	110

Page

Frame Averaging..... 110
Smoothing..... 111
Contrast Enhancement..... 112
Enhancement by Linear Transfer Function... 112
Enhancement by Non-Linear Transfer Function (Histogram Modification)..... 113
Edge Enhancement..... 130
Discussion..... 134

VI CONCLUSION..... 141

APPENDICES

A RECONSTRUCTION ALGORITHM..... 147

B POINT SPREAD FUNCTION..... 160

REFERENCES..... 164

BIOGRAPHICAL SKETCH..... 170

Abstract of Dissertation Presented to the Graduate School of the University of Florida in Partial Fulfillment of the Requirements for Degree of Doctor of Philosophy

REAL-TIME PORTAL IMAGING OF MEGAVOLTAGE THERAPEUTIC PHOTON BEAM

By

Mohammad Khairul Islam

December, 1987

Chairman: Francis J. Bova, Ph.D.
Co-Chairman: Lawrence T. Fitzgerald, Ph.D.
Major Department: Nuclear Engineering Sciences

The feasibility of a real-time digital imaging system for radiation therapy localization and verification has been evaluated. Two different imaging approaches were investigated, one based upon a video-fluoroscopic system and the other upon a coded aperture device. The fluoroscopic system utilized a fluoro screen, a low-light video camera and a frame grabber to digitize an image. The image was processed to optimize anatomical visibility. This system produced images with similar contrast to those of port films. However, since all the components of this prototype system are contained in a light-tight box of 50 cm x 50 cm x 100 cm in size and which must be positioned at the exit side of the radiation portal, its use was limited to only some selected clinical situations.

The other prototype imaging device utilized a strip ion chamber, 22 cm in length, 2 mm in width, with a separation of 2 mm between the front and rear electrodes. Strip

projections of the radiation portal were collected by translation of the detector in 1.98 mm intervals across the radiation field. Multiple views were obtained by rotating the detector strip and taking a projection at angular increments from 0 to 180 degrees. A minicomputer was used to control the data acquisition electronics and detector movements. The images were reconstructed from the projection data by use of a filtered back-projection algorithm. A frame grabber was utilized to display the video images. Enhanced images were obtained by digital image processing. Both air and a liquid (iso-octane: 2,2,4 trimethyl pentane) were evaluated as detector ionizing media. The images obtained with the liquid ion chamber were found to be of higher contrast than those with the air chamber. The point-spread function of the entire system, with iso-octane as the ionizing medium, was determined to be 4.2 mm. The collection efficiency of the liquid ion chamber was estimated to be about 50% at a field strength of 1.0 kV/mm. The signal-to-noise ratio of the ionization current signal was 2500:1. Images obtained with the liquid ion chamber and a cobalt-60 source were compared with those obtained with the metal-screen-film cassette and were found to have better contrast. The performance of this prototype suggests that a practical imaging unit, which would employ multiple strip ion chambers, would be capable of generating portal images in five to ten seconds.

CHAPTER I
INTRODUCTION

There are several factors involved in the course of radiation treatments which tend to compromise accuracy. Such factors include patient movement, improper placement of radiation blocks and shifting of skin marks relative to internal anatomy. All of these factors result in incorrect beam alignment. At present, the only method of verifying and documenting the extent of geometric accuracy employs a radiotherapy portal film.

Prior to treatment, the patient setup is determined utilizing a therapy simulator. The target area is identified and a diagnostic quality radiograph is taken. Shielding blocks are designed and fabricated to restrict the therapeutic beam to the tissue at risk. Before irradiating with the therapy beam, positioning of the patient is verified by obtaining a portal radiograph commonly called a port film. Port films taken with the therapeutic beam are of lower contrast than diagnostic films due to noncoherent scattering at megavoltage energies, weak dependence on atomic number (Z), large source size (for cobalt units), patient movement due to long exposure time, beam edge unsharpness due to thick collimators and poor exposure techniques (Reinstein et al. 1984).

The accuracy of the treatment is determined by comparing the patient's port film and simulation film. Since the time required for exposure, development and evaluation of a port film is on the order of five to ten minutes, daily radiographs are utilized for verification only in selected cases.

The difference in the anatomical coverage of the intended treatment field and the irradiated field is termed localization error. The poor quality of port films and their infrequent use can allow localization errors to persist throughout the course of treatment without detection. Studies (Haus and Marks 1973, Byhardt et al. 1978, Marks et al. 1978) have shown that a localization error of 0.5 cm or greater can occur in as many as 50% of the more complex fields and about 15% when averaged over all anatomical sites. These errors have been implicated as a cause of failure to locally control the tumor (Chu and Fletcher 1973, Glinas and Fletcher 1973). Therefore, daily imaging of the treatment field is indispensable if the precision of modern radiation therapy equipment is to be fully utilized.

The aim of this work was to investigate the feasibility of developing a real-time digital portal imaging system. A real-time system would make daily portal imaging practical while a digital format would enable enhancement techniques to be used for optimizing image quality. A video fluoroscopic system, which

incorporates a fluoro-screen, a low-light video camera, a frame grabber and digital image processing was studied.

Another system, a coded aperture imaging device (CAID) utilizing a strip ion chamber was developed. The projection data of the portal were collected by translate-rotate movement of the chamber. The image was reconstructed from the projection data by a filtered back-projection algorithm (Ramachandran and Laksminaryanan 1971). Air and liquid iso-octane were investigated as the ionizing media.

CHAPTER II
BACKGROUND

Many techniques have been employed to improve the contrast of port film images for the localization and verification of radiotherapy treatments. Attempts have also been made to replace port film imaging with alternative imaging methods.

Efforts to improve the contrast of portal films through the careful choice of metal screens incorporated into the film cassettes (Hammoudah and Henschke 1977, Droege and Bjarngard 1979a, 1979b) have yielded small improvements. The simple photographic technique described by Reinstein and Orton (1979) and Reinstein et al. (1987) which involved making a reversal contact print of the original film onto an ordinary x-ray film, yielded enhanced image contrast by gamma multiplication. Similar results have been achieved using digital image enhancement techniques (Leong 1984, Meertens 1985, Shalev and Arenson 1984). These systems digitized the film by using a high quality low-light video camera or a scanning densitometer. The processing of the data utilizes a graphic processor or digital imaging computer. Another method of obtaining enhanced portal films reported by Wilenzick et al. (1987), involved digital enhancement of images obtained by a computed radiographic imaging (CRI)

system. The CRI system is based on the principle of laser-stimulated luminescence induced in an image receptor plate exposed to ionizing radiation and direct conversion of the light image into digital form. Although the processed images were visually pleasant, they did not provide more information than the original image. Furthermore the image enhancements required processing time.

In recent years, several methods of real-time digital imaging have been proposed. One such system is a video fluoroscopy system, described by Baily et al. (1980). This system consisted of a Dupont E-2 fluorescent screen in contact with a 1/16" stainless steel buildup plate. The screen fluorescence was detected by a low-light video camera. The video system incorporated an f-0.78, 13 mm focal length lens and a silicon intensified vidicon imaging tube. The system was able to obtain acceptable images of the treatment portal in real-time. The system produced superior images with the 6 MV x-ray than when cobalt-60 was used. The improvement at 6 MV was attributed to the smaller focal spot size of the 6 MV source as compared to that of the cobalt unit.

Leong (1986) has reported a similar video fluoroscopic system which incorporates digital image processing techniques. His imaging section followed the design of Baily et al. The image processor (Trapix 55/88) was a real-time digital system with an 8-bit frame grabber. This unit was capable of digitizing a frame into a 512x512 pixel buffer at

normal video frame rate. The image processor also performed a host of mathematical and logical operations at normal frame rate. The images obtained were described to be of good quality, but no attempt to optimize various components of the system in terms of clinical performance and cost was reported.

Electronic portal imaging by direct radiation detection and subsequent signal processing for visual display has been described by Tabrosky et al. (1982) and Lam et al. (1986). Their system consisted of a linear array of 256 silicon diodes with a center-to-center separation of 2 mm. The radiation field was scanned with the diode array in 2 mm steps. The detector movement and the data collection were under computer control. Analog signals were digitized by an analog-to-digital converter (ADC) to generate the digital image. The quantum efficiency of the silicon diodes was reported to be 3% and the signal-to-noise ratio (SNR) of the system was reported to be 119:1. The quality of the phantom images was described as comparable to those of the port films. The performance of this device however, would be limited by the electronic noise. Also, long term stability of the semiconductor diode due to possible radiation damage, related cost factors and overall clinical performance of the system remained to be evaluated.

Meertens et al. (1985) have described an imaging device which utilized a liquid for radiation detection. The

imaging area of the system was a matrix of ionization chambers filled with iso-octane (2,2,4-trimethyl pentane). The ion chamber matrix consisted of a front plate and a rear plate, each containing 32 equally spaced electrode strips. The orientation of the plates was such that the collecting electrodes on the rear plate were orthogonal to the high voltage electrodes on the front plate. The high voltage was connected to each front strip and the integrated ionization current of each of the detector strips was measured to obtain one profile of the radiation field. The whole imaging area was scanned by switching the high voltage to each of the front strips and obtaining the corresponding profile. For a front-rear strip separation of 1.0 mm, a strip width of 1.27 mm and a field strength of 250 volts/mm, the SNR of the system was 200:1. The image qualities of test phantoms were reported to be similar to those of port films. Improvement of the image contrast would require a higher SNR which, in this system, requires the application of higher field strength. The design of a high voltage switching system for a very high field strength was complicated and expensive, and therefore the authors did not employ higher field strengths. According to the authors, the prospect of obtaining improved spatial resolution with this design is also limited. If the strip width and separation between strips were reduced, images would have more blurring due to the effect of the angular distribution of secondary electrons.

Verification and localization by portal films have some inherent limitations. They require a relatively long time to process and thus weaken the link that is so important in such a feedback system. Due also to the inherent low contrast, a considerable amount of time is required to view and interpret port films. While enhanced film images offer superior object detectability in shorter time compared with unenhanced films, they require extra time for image enhancement.

The potential advantages of a real-time digital imaging system are many. The display of the ongoing treatment portal on the video monitor can reveal errors in the patient position which occur during treatment and thus will allow the operators to take corrective action when it is needed. The digital data can be manipulated by using digital image enhancement techniques to yield a higher quality image. Moreover, digital image data can be stored on a magnetic medium and can be retrieved quickly for comparison. All these features give real-time digital many advantages over conventional radiography and hence the investigation into the development of a real-time imaging device for radiotherapy localization and verification is of great interest.

CHAPTER III
THE FLUORO SYSTEM

With the availability of efficient low-light video cameras and digital image processing techniques, digital fluoroscopy appeared to have potential as a real-time imager for high-energy photon beam radiation therapy. An attempt was made to analyze and evaluate the performance of a digital fluoroscopic system as a real-time imaging unit for portal verification and localization.

The advantage of digital fluoroscopy as a real-time portal verification and localization system is its relative simplicity. This imaging system utilizes a fluoro-screen to convert the x-ray image to a light image. The light image is then detected by a video camera. The video image can then be digitized. The digital image can be manipulated by digital image processing techniques in an attempt to enhance the latent information of the image.

System Description

The schematic diagram of the fluoroscopic portal imaging device is shown in figure 3-1. The imaging section closely followed the design described by Baily et al. (1980). To avoid direct irradiation of the camera by the photon beam and to minimize the physical size of the

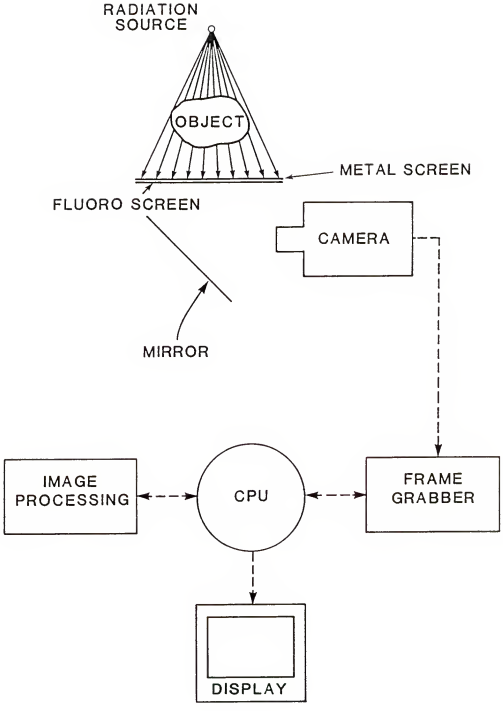

Figure 3-1. Schematic diagram of the fluoroscopic portal imaging device.

system, the light image was bent by 90 degrees through the use of a front surface mirror. The imaging system (fluoro-screen, the mirror and the camera) was mounted in a box to exclude room light. The video signal from the camera became the input to the computer-controlled frame grabber which digitized and stored the image data for processing. A detailed description of each of the components follows.

Fluoro-Screen

The conversion of x-ray energy to light occurs in two stages. In the first stage the absorbed x-ray energy is converted to high-energy electrons. In the second stage the kinetic energy of the released electrons is converted to light.

The basic function of the fluoro-screen is to convert the radiation energy to light energy. The exact detail of the energy conversion to light may be different for different phosphors. In general, part of the radiation energy is used to produce excited states within the material. Light emission occurs when the excited states return to their normal state. The light emitted instantaneously (within 10^{-8} seconds of stimulation) after the introduction of the excitation energy is called fluorescence. Fluorescence is associated with the presence of localized energy levels in the normally forbidden energy gap in the energy band of the phosphor. The localized

energy levels, called the luminescent center, are usually produced by an activator atom which is an imperfection intentionally added to a pure crystal. The activator atoms vibrate about their equilibrium position and as a result the emitted photons are not monoenergetic but rather a spectrum of light is emitted.

A fluoro-screen is composed of a smooth layer of phosphor on a substrate coated with a thin film of aluminum. Typically, the thickness of the layer of luminescent material is less than 10 μm with the phosphor particles from 1 to 5 μm in size. The efficiency of the fluoro-screen is determined by the thickness of the screen, by the losses in the aluminum coating, by the size of the phosphor particle and by the compton electron energy. In general, the larger the particle size of the phosphor, the greater the screen conversion efficiency. The loss in the aluminum film may be minimized by keeping the film as thin as the opacity requirement allows. The thickness of the phosphor screen is critical as far as efficiency is concerned. If the phosphor screen is too thin, the compton electrons are not stopped by the fluorescent material but passes through it giving up energy to the substrate material. Conversely, a phosphor layer thicker than the penetration depth of the compton electron absorbs some light as light passes through the material. The resolution of the screen depends only on thickness and not on particle size. In the case of very thin screens however, the resolution is

reduced with increased particle size; where the thickness of the phosphor particle becomes the limiting factor (Csorba 1985).

The important parameters of the fluoro-screen include (1) the absorption efficiency as a function of energy (2), the intrinsic conversion efficiency from X-ray energy to photon energy, (3) the matchup of emission spectrum with photocathode sensitivity of the camera and (4) the screen losses due to isotropic emission and self absorption. Several screens including MCI PFG(ZnsCds:Ag,cl), Dupont QUANTA III(LaoBr:Tm) and 3M TRIMAX-12(Gd_2o_2s:Tb) were used for imaging experiments. Among these the TRIMAX-12 has a higher phosphor coating density, 110 mg/cm^2, as opposed to 55 mg/cm^2 for the other two screens. The TRIMAX-12 was found to yield highest light output and best image contrast.

Metal Screen

The use of a metal screen in front of the fluoro-screen served a dual purpose, it provided electronic buildup and minimized the contribution of scatter. A metal screen alters the scatter-to-primary ratio (S/P) due to differences between the primary and scattered photon energy spectra. The screen affects the relative transmissions of energy fluence for these spectra.

Influence of scatter on contrast. It is the spatial variation of X-ray fluence which is responsible for the

intensity variation in the radiographic images. Figure 3-2a illustrates the process. The step in the phantom causes a difference in transmission of the photon fluence. This differential transmission gives rise to an intensity difference in the image. The contrast in the image could be represented by

$$C_i = kf(C_s) \tag{3.1}$$

where k is some proportionality constant, and C_s is the subject contrast defined by

$$C_s = (P2-P1)/(P1+S). \tag{3.2}$$

In equation (3.2) P1 and P2 are the doses due to the primary photons, i.e., those photons which penetrate the object without interactions. The photons which do interact and are deflected to the detector at some angle contribute to the second order effect, the scattered dose S. For a small spatial object it is assumed that S is the same on both sides of the step and therefore the difference in the primary dose P'=P2-P1 is responsible for the intensity difference in the image. Equation (3.2) could be rewritten as

$$C_s = P'/[P(1+S/P)] \tag{3.3}$$

where P1 was rewritten as P. Equations (3.1) and (3.3) indicate that fluoroscopic contrast can be modified by modifying k or S/P or a combination of both. The parameter

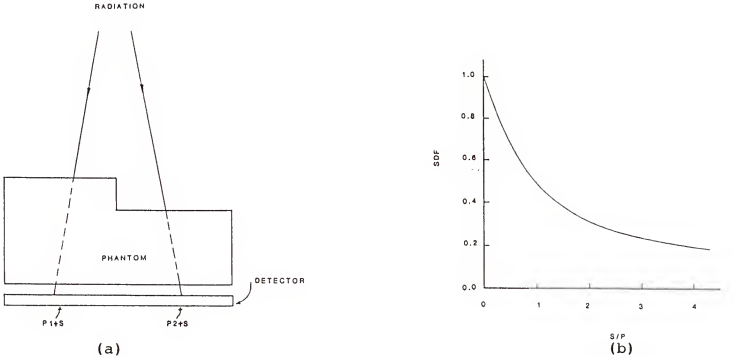

Figure 3-2. Influence of scatter on contrast: (a) low contrast step phantom, (b) plot of SDF vs. S/P.

k is analogous to film gammma, it is a unique characteristic of the fluoro-screen. Thus, for a particular fluoroscopic screen, the image contrast can be improved by minimizing the S/P value.

The contrast reducing effect of scatter is a well known phenomenon, but it is not usually obvious that a relatively small amount of scatter will result in a significant loss of contrast. This fact can be illustrated by rewriting equation (3.3) in terms of the scatter degradation factor (SDF) (Barnes 1979).

$$C_S=(P'/P)\ SDF \tag{3.4}$$

where

$$SDF=1/(1+S/P). \tag{3.5}$$

A plot of SDF vs. S/P is shown in figure 3-2b. The value of SDF represents the fraction of primary beam contrast imaged. To illustrate, for S/P value of zero one hundred percent of the primary beam contrast will be imaged, but if S/P value is unity only 50% of the primary beam contrast will be imaged. In an attempt to minimize the S/P value an optimum front screen was experimentally determined.

Optimization of the front metal screen. An optimum thickness for the metal screen in front of the fluoro-screen was determined by estimating the S/P value. Experimental data were obtained with a cobalt-60 source. A uniform 10 cm thick water phantom was used to provide the scatter. The

imaging device was set up as shown in the schematic diagram (figure 3-1). To estimate the S/P for a particular screen thickness, digital images of the uniform water phantom were obtained for various field sizes. The average of 16 frames was taken to minimize the random noise and an average value of four pixels at the geometrical center of the frame was taken as a measure of primary plus scattered radiation. Plots of the average pixel value vs. field size were generated for different thicknesses of the metal screen (figure 3-3). From these plots, values due to primary radiation alone were estimated by extrapolation of the curves to zero field size. Thus, the scatter contribution for any field size was determined by subtracting the primary value from the primary plus scatter value. Figure 3-4 shows a plot of S/P as a function of screen thickness for a field size of 20 cm x 20 cm. From the figure it is obvious that with increasing lead thickness the S/P value decreases rapidly at first and then it decreases slowly.

Since the low energy scattered photons are readily absorbed by the lead, scatter (S) decreases as the lead thickness is increased. The attenuation is rapid at first and then less dramatic as the lowest energy scattered photons are preferentially absorbed. For thick screens S/P continues to decrease slightly due to the greater attenuation of the scattered compared to the primary photons. Eventually, the scattered photon spectrum is filtered of its low energy components and further increases in screen

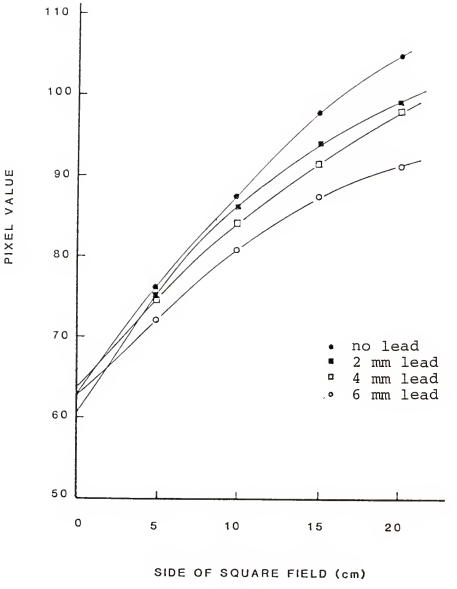

Figure 3-3. Primary plus scatter value as a function of square field size for different thicknesses of lead (in combination with 1.7 mm aluminum).

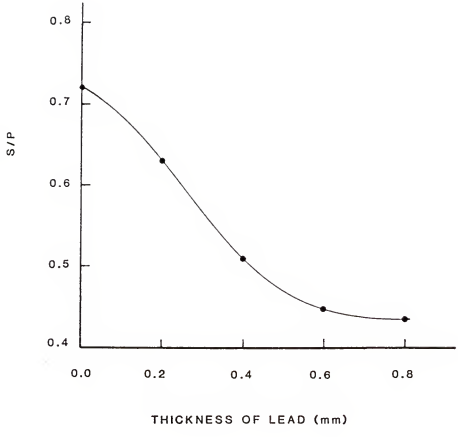

Figure 3-4. Scatter to primary ratio as a function of lead thickness (in combination with 1.7 mm aluminum).

thickness have a negligible effect on the S/P value. A thick metal screen also absorbs the higher energy electrons generated in the phantom and thus offers higher resolution. A combination screen of lead and aluminum was used to take advantage of the fact that lead preferentially filters out the scattered photons while the aluminum provides a less energy dependent response for the unfiltered photons.

A screen consisting of 0.6 mm lead and 1.7 mm aluminum was found to give an optimum S/P, with cobalt-60 radiation, without excessive reduction of the primary beam. This result agrees well with the result of Droege and Bjarngard (1979a) who studied the influence of metal screens on the contrast of port film images. They found that a combination screen composed of 0.51 mm lead and 1.5 mm aluminum yields a minimum S/P value.

Video Camera

The choice of the camera system is perhaps the most critical aspect of fluoroscopic imaging. Since the present problem deals with imaging in a low-light condition (on the order of 10^{-3} foot-candle), an efficient light sensitive camera would be a logical choice.

Camera tubes are electro-optical devices that are used to detect the optical image of a scene and to convert the detected image into electrical signals suitable to be televised. The most commonly used devices operate on the

charge image principle. In this case the tube consists of a photocathode and an image storage target for conversion of the incident radiant energy into an electrical charge image pattern corresponding to the imaged scene. An electron beam scans the target reading out the charge pattern as a time-based video signal (Csorba 1985).

In the most simple case the image storage section consists of an optically excitable camera tube target i.e., a photoconduction type target. In more sophisticated camera tubes, however, the storage target is in the image plane of an image intensifier tube, i.e., the optical image of the scene is either intensified or converted to a high energy electron image. The readout section consists of a biaxially deflected low-energy electron beam with the associated video output components. Frequently the video signal is obtained directly from the signal plate of the storage target. In other instances, however, the video signal is obtained as an amplitude modulation of the scanning beam that is returned by the storage target and amplified by an internally arranged photomultiplier tube.

For the purpose of present investigation the desired characteristics of the camera should include (1) the best matchup of the photocathode sensitivity with the emission spectrum of the fluoro-screen, (2) high current gain in low light conditions and (3) band width compatible to that of the ADC of the frame digitizer, i.e., satisfies the Nyquist criteria.

Three different low-light cameras, the Panasonic WV-1550, the Philips XTV-5 and the MTI SIT-66 were experimentally evaluated. The Panasonic WV-1550 camera has a newvicon imaging tube (photoconduction type) with a spectral sensitivity ranging from 400 nm to 950 nm and with a peak in the neighborhood of 700 nm (infrared). Since the spectral peak of the fluoro-screens under investigation was around 550 nm and the target did not have any image intensification mechanism, this camera showed poor performance. The Philips XTV-5 camera, which is routinely used in diagnostic fluoroscopy, was also evaluated next. This camera employs a plumbicon imaging tube, it is also of the photoconductive type and shows peak sensitivity around 600 nm providing a better match with the emission spectrum of the screen than the Panasonic system. The plumbicon tube also offers better contrast characteristics than that of the vidicon tube. As expected, the Philips system yielded images with higher contrast than those of the Panasonic system.

Finally, the performance of a silicon intensified target (MTI SIT-66) camera was evaluated. The tube of this camera has an image intensification mechanism. The charge storage target is in the image plane of an image intensifier tube. The video signal is obtained as an amplitude modulation of the scanning beam that is returned by the storage target and amplified by an internally arranged photo-multiplier tube. The target gain of the SIT camera is

of the order of 2000 to 2500. The high target gain enables the SIT tube to operate at a lower light level than any other conventional camera.

With this camera a usable image can be obtained down to a face plate illumination level of approximately 1.0×10^{-5} foot-candle, whereas for conventional image tubes this value is approximately of the order of 10^{-3} foot-candle. The photocathode of the SIT tube shows a peak sensitivity around 450 nm. The images yielded by the SIT camera were found to be of higher contrast than those of the other two cameras described earlier.

Frame Grabber

The frame grabber is a Model 274C Video Frame Store manufactured by Colorado Video Inc. It has a solid state video memory with high speed analog-to-digital (ADC) and digital-to-analog converters and is capable of digitizing, storing, and displaying a single frame of video information in real-time. It utilizes a standard 2:1 interlace and outputs a composite video of 1 volt peak-to-peak. It has a resolution of 512x512 picture elements with a video bandwidth of 5 MHz and a grey scale 8 bits deep (256 levels).

The controls of the Model 274C include black level control and video level control. The black level controls the DC level of the video signal going to the internal ADC.

This can be set to such a level that the detail of the black portions of the input signal are not lost. The video level, on the other hand, controls the amplitude of the video signal going to the internal ADC. This can be set to such a level that white details of the input signals are not compressed. Both the black level and the video level controls were adjusted to obtain an optimum image.

Image Processing

Image processing software in the spatial domain was written and was applied to video images utilizing a PDP-1134 computer. The algorithms of the image processing software include frame averaging, smoothing, linear contrast enhancements, histogram modification and edge detection. Descriptions of these image processing algorithms are given in Chapter V.

System Performance and Results

A quantitative evaluation of the system performance would require basic data of the individual components. Unfortunately, for the fluoro-screen and the photocathode material of the camera, no data in the megavoltage energy range were available. Therefore, the system performance and the system noise will be discussed only qualitatively.

System Efficiency

The detection elements which determine the overall efficiency of the system are the fluoro-screen, the collection optics, and the photocathode material of the camera tube.

As mentioned earlier, the important screen parameters are the (1) absorption efficiency (A) as a function of energy, (2) the intrinsic conversion efficiency (C) from X-ray energy to visible photon energy, (3) matchup between screen output and camera photocathode sensitivity (X=number of electrons ejected from the photocathode/ number of light photons) and (4) screen loss due to self absorption (L).

In the diagnostic energy range, the absorption efficiency of the Trimax-12 screen is approximately 30%, while the intrinsic conversion efficiency is approximately 18% (Curry et al. 1984). A typical value of screen loss is about 50% (Curry et al. 1984).

To estimate the X-ray absorption efficiency of the Trimax-12 screen in megavoltage energy transmissions measurements were made utilizing a good geometry. The measurements were made with a cobalt-60 source and a Markus chamber. A build-up of 0.5 cm of Solid Water® was used above the chamber. Measurement values with and without the fluoro-screen in the radiation beam yielded the absorption efficiency of the screen, which was found to be 8.6%.

Another experiment was performed in a contact geometry to estimate the fraction of electrons absorbed by the phosphors in the screen. The fluoro-screen was positioned on the top of the chamber and 0.5 cm of Solid Water® was placed on the top of the screen to provide electron buildup. Measurements were made with the intact screen and then with phosphor particles removed. These two measurements yielded an estimation of electron absorption efficiency of the phosphor particles; which was found to be 9.0%. Thus, it was estimated that the overall detection efficiency of the fluoro-screen in megavoltage energy range is less than 1%.

Besides the low X-ray detecting capability of the screen, the weak link of the system is the optical coupling efficiency (E) between the screen and the camera tube. The factor (E) is determined by (1) the magnification (M) required to transfer the input image onto the photocathode of the camera, (2) the lens speed or f-number (F), (3) the transmitivity (T) of the lens and (4) the reflectivity R of the front surface mirror.

The optical coupling efficiency (E) in terms of the factors discussed above is given by (Nelson et al. 1982)

$$E=M^2TR/[(1+M)^2 4F^2]. \qquad (3.6)$$

To illustrate, for F=0.7, T=0.9, R=0.95 and for a typical magnification M=(3.6 cm/ 38 cm), the value of E becomes 0.003.

The overall transfer efficiency (G) of the system can be expressed by

$$G=(0.5WCL)XEA$$
$$=QXEA \qquad (3.7)$$

where W is the average X-ray energy per average output photon energy and the term Q represents the number of visible quanta per unit X-ray photon. The factor 0.5 takes the isotropic nature of the light emission into account. Equation (3.7) suggests that the light level available to the camera is further lowered due to the poor collection ability of the optical system.

System Noise

To study the system noise the statistical nature of each of the elements needs to be taken into account. The imaging system can be considered as a multiplicative chain and the components can be grouped to the statistical distributions which characterize them. It can be assumed that the number of X-ray photons (N) incident per unit area and the factor Q are variables with Poisson distributions. The variables A, E and X can be characterized by a binomial distribution (Nelson et al. 1982). According to the formulation of Albrecht (1965) the noise power for the alternative chain consisting of Poisson and binomial processes is given by

$$\sigma^2 = NAQEX(1+AQEX+QEX). \qquad (3.8)$$

With the output signal given by

$$S = (N)AQEX \qquad (3.9)$$

the signal-to-noise ratio (SNR) of the system becomes

$$SNR = (N)^{1/2}(AQEX)^{1/2}/(1+AQEX+QEX)^{1/2}. \qquad (3.10)$$

Equation (3.10) suggests that the system SNR is not limited by the absorption efficiency of the screen alone. It has some weak dependence upon other factors, such as the screen emission characteristics, the spectral bandpass of the lens and the spectral sensitivity of the photocathode of the camera. Equation (3.10) shows that the SNR value is proportional to the square root of the number of X-ray photons (N) and thus suggests that the value of SNR could be improved by frame averaging.

The effect of noise reduction by frame averaging was evaluated by grabbing multiple frames with a cobalt-60 flood source and averaging them. The system noise was estimated from the standard deviation of the pixel values (Leong 1984). A plot of standard deviation vs. number of frames taken in the averaging is shown in figure 3-5. Initially the system noise reduces rapidly with the number of frames averaged. It then begins to reduce more gradually and finally attains almost a constant level at about an average of 16 frames. This lower limit of the system noise is due

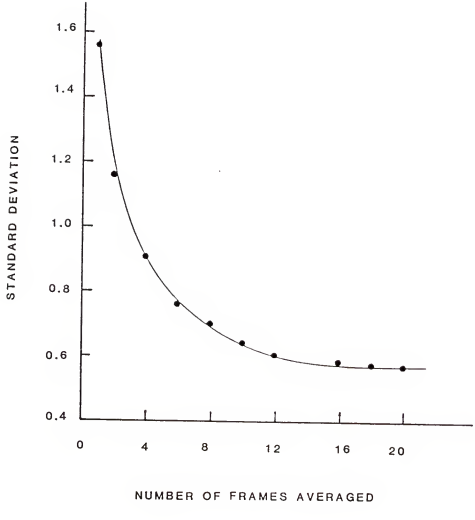

Figure 3-5. Reduction of noise by frame averaging.

mainly to the noise associated with the camera system as suggested by equation (3.10).

Images

By averaging multiple frames, images with reduced statistical noise were obtained. As suggested by the plot of noise vs. number of frames, an averaging of sixteen frames was found to yield an optimum image. Figure 3-6 shows the images of a cow vertebrae obtained with the Philips camera and cobalt-60 radiation. It shows the comparison of a single frame image and a 16 frames averaged image. Photograph of the cow vertebrae is shown in figure 3-7.

Various phantom images were obtained with an MTI SIT-66 camera, which was connected with a noise reduction unit. The noise reduction unit allowed averaging of multple frames of images before displaying them on the video monitor. With this unit an average of sixteen frames was again found to yield an optimum image.

Images obtained with the SIT camera system were averaged by sixteen frames and video taped. Imaging experiments were performed with a cobalt-60 source and 8 and 17 MV x rays from a Philips SL 75-20 linear accelerator (Linac). Images obtained with the Linac were found to be superior to those obtained with cobalt-60. This is primarily due to the smaller focal spot size of the Linac. The Linac

Figure 3-6. Fluoro images of the cow vertebrae: (top) single frame, (bottom) average of 16 frames.

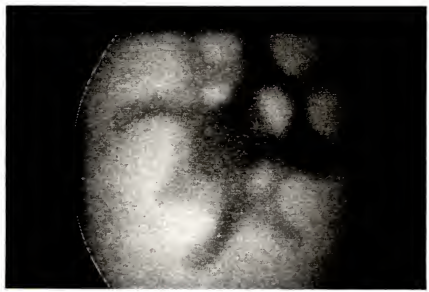

Figure 3-7. Photograph of the cow vertebrae.

focal spot size is approximately 2 mm while the cobalt source is approximately 2 cm in diameter.

To study the clinical performance of the prototype, a lateral view of the radiation portal of an ongoing head and neck treatment was imaged and video taped. The patient was treated with 8 MV X-rays. Figure 3-8 compares the fluoro image with the port-film image. The quality of the fluoro image, as reproduced here, has been degraded somewhat due to the noise associated with the video taping procedure. As can be seen from the figure the fluoro image has similar contrast to that of the film image.

Enhanced Images

To study the effectiveness of the image processing techniques, on fluoro images, described in Chapter V, an image of a human skull obtained with 8 MV x rays was used. Due to the presence of noise contrast enhancement using the full dynamic range did not produce a visually pleasant image. Contrast enhancement through clipped adaptive histogram equalization (AHE) technique, however, was found to yield images of higher contrast. This technique enhances the contrast to a limited degree and hence deters overenhancement of the noise. Edge enhancement techniques also, did not perform well on the fluoro images due to noise. A detailed discussion of enhancement of images is presented in Chapter V.

Figure 3-8. Images of a lateral view of patient's head and neck portal: (top) film image, (bottom) fluoro image.

Discussion

The work reported above used video camera systems on loan and thus detailed investigation of performance of system components was not possible due to the limited availability of the equipment. However, the images obtained with the prototype fluoro system were found to be comparable to conventional port film images. Digital image processing techniques could be utilized to obtain enhanced contrast if the images contained low noise. To improve the SNR of the fluoro images the radiation collection efficiency of the overall system needs to be improved through optimizing the various components.

Looking at the expressions for overall transfer efficiency (equation 3.7) and SNR (equation 3.10), it is clear that the system performance can be improved in three different areas: (1) the fluoro-screen, (2) optical coupling and (3) the camera target.

The characteristics of the screen which can be optimized are (1) X-ray absorption efficiency, (2) light output losses and (3) matching of spectral output with the sensitivity of the photocathode material of the camera tube.

Besides the intrinsic efficiency which depends upon the chemical composition, the efficiency of the phosphor screen is largely determined by the screen thickness, particle size of the phosphor and beam energy. The

resolution is however largely dependent upon the screen thickness. The use of a larger particle phosphor with a thin screen results in loss of resolution. A suitable compromise between resolution and efficiency is to make the diameter of the phosphor particle equal to the thickness of the screen (essentially a monolayer screen).

The optical coupling efficiency (E) (equation 3.6) is strongly dependent upon the magnification as $M^2/(1+M)^2$. Calculations show that an increase of approximately 30% in the coupling efficiency is achieved if a field of view of 33 cm rather than 38 cm is projected onto a 3.6 cm diagonal photocathode. On the other hand, if the field size is to remain the same, a larger size photocathode would improve the efficiency by a considerable amount.

As is evident from equations (3.7) and (3.10) the overall efficiency and SNR also depend upon the factor X, which is a measure of the number of electrons produced in the camera tube target per unit light photon. Clearly, camera tubes having intensifying capabilities yield much larger values of X than those of conventional photoconductive camera tubes. The selected camera should have a lens with an antireflective coating and the peak transmission wavelength should correspond to the peak of the emission spectrum of the screen.

CHAPTER IV
THE CODED APERTURE IMAGING DEVICE

As discussed in Chapter III, the overall detection efficiency of the fluoro-screen in the megavoltge energy range is less than 1%. The overall system efficiency of the fluoro system is further degraded by the low optical coupling efficiency. To achieve a higher signal strength for megavoltage imaging a search for an alternate detecting medium was in order.

A solid-state detector system, having high absorption efficiency was one consideration. A two-dimensional matrix of small solid state detectors could be used to produce an image, where the signal from each individual detector would represent a pixel. In this design, however, there are practical problems. For example, if each detector were to represent an image element of 2 mm x 2 mm, a total of 40,000 detectors will be needed to image a field of view of 40 cm x 40 cm.

To overcome the difficulties of handling such a large matrix of individual detectors, the use of an array of solid-state strip detectors, with length-wise uniform response, can be utilized. This type of detector design would collect data in a coded aperture format. The signal produced by each strip detector would be equivalent to the

summation of signals produced by a linear array of small detecting elements. The signal data produced by all the strip detectors in a particular orientation would produce one projection of the field of view. The image would have to be recontructed using multiple projection data by an image reconstruction algorithm.

A prototype coded aperture device (CAID), consisting of a single strip detector, which is capable of collecting projection data by translation and rotation was developed. The image reconstruction process of this device is identical to that used in the first generation CT except that the ray-sum in the present case represents the sum of pixel intensities along a ray line, while in CT it represents the sum of X-ray absorption coefficients of the pixels along a ray line. This principle was described previously (Luthmann 1978, Mauderli et al. 1979, 1981, Urie et al. 1981, Mauderli and Fitzgerald in press) for photon emission imaging in nuclear medicine.

System Description

The schematic diagram of the CAID is shown in figure 4-1. The data acquisition of the system was accomplished by utilizing a long-narrow strip detector. The projection data for each view of the portal were collected by translating the detector through the imaging field. The translation of the detector simulated a device which would

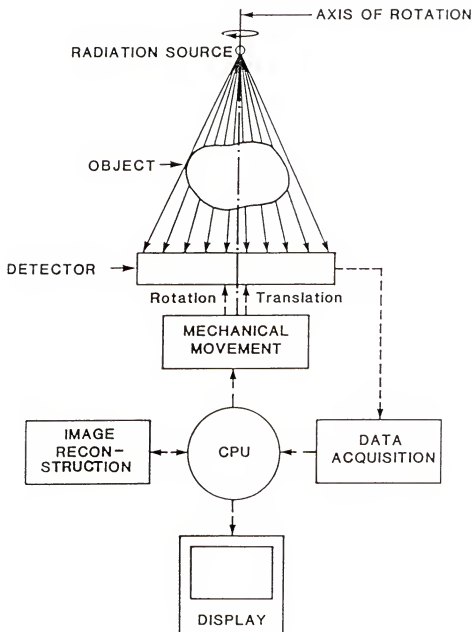

Figure 4-1. Schematic diagram of the coded aperture imaging device.

have many strip detectors allowing instantaneous collection of the projection data at each viewing angle. Projection data for multiple views between 0 and 180 degrees were obtained through a sequence of rotation about the geometric center and translation of the detector. A microcomputer was used to control the mechanical motion and data acquisition electronics. The image was reconstructed by a filtered back-projection algorithm (Ramachandran and Laksminaryanan 1971). The resultant image was displayed on a monitor by utilizing a video frame grabber. A description of each of the components of the imaging device follows.

Radiation Detector

The choice of the strip detector should include the following charcteristics: (1) high quantum detection efficiency, (2) linearity, (3) uniformity of response along the detector length, (4) high speed of response, (5) optimum dynamic range, and (6) stability. The choice of a detector system also depends upon factors such as cost, ease of construction and ease of handling.

A strip of plastic scintillator, 2 mm wide, 6 mm high and 350 mm long, was evaluted as the potential radiation detector. The plastic scintillator was chosen because of its geometrical uniformity and high radiation absorption efficiency. Under the influence of radiation, the scintillator emitted visible light photons with a wavelength in the

range of 575 to 700 nm, which were then converted to electrical signals by photodiodes. The peak response of the photodiode was around 900 nm. However, the photodiodes were found to be extremely sensitive to scattered radiation and as such introduced noise into the projection data. The SNR of this detector system was 60:1. This was determined from the standard deviation of measurements at a fixed position in the field of view. The images obtained by this detector were found to be of very low contrast and high noise (shown in figure 4-22). The scintillator detector system was therefore abandoned, without further measurements, in favor of a more suitable detecting system.

The next consideration for a detector was a liquid ionization chamber. It was chosen for its uniformity of response, wide dynamic range and high radiation absorption. A parallel plate strip ion chamber was designed and fabricated. Both liquid iso-octane and air were evaluated as the ionizing media.

Chamber design

The design of the parallel plate strip ion chamber is shown schematically in figure 4-2. The chamber was 220 mm long and the collecting electrode was 2 mm wide. Separations of 2 mm and 6 mm between electrode plates were evaluated. The electrodes were made from copper-plated circuit boards. A uniform separation between the high

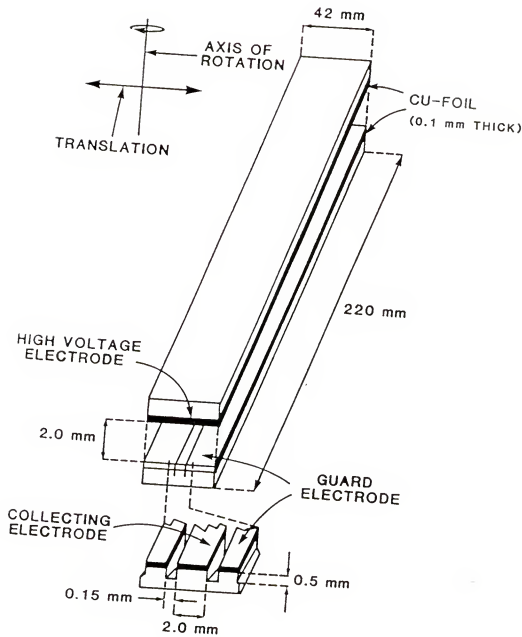

Figure 4-2. Schematic diagram of the parallel plate strip ion chamber.

voltage and collecting electrodes was maintained by an accurately machined Rexolite® spacer. Rexolite®, a styrene co-polymer, has good chemical tolerance to iso-octane and has excellent dielectric properties which are not significantly affected by radiation (Wickman 1974). The electrodes were glued to acrylic plates of 6 mm thickness to provide mechanical support and to obtain electronic build-up on the front-surface plate. The total build-up above the sensitive volume of the ion chamber was about 0.79 gm/cm^2. The front and rear plates, with their conducting surfaces facing each other were cemented to the Rexolite® spacer. Two small holes were drilled at one end of the chamber to allow subsequent filling with liquid.

The guard electrodes were used to prevent leakage current from the high voltage electrode to the collecting electrode. These electrodes were maintained at the same potential as that of the collecting electrode in order that they may not themselves become a source of leakage current.

The design of this ionization chamber has the advantage of low cross-talk between the charge collecting volume and the neighboring volume. The electric field lines between the high voltage and collecting electrodes are perfectly parallel to each other and thus the charge collecting volume is well defined.

Ionizing medium

Air was the first ionizing medium to be evaluated. The air chamber had the advantage of a high speed of response and high collection efficiency (as discussed in the next section) but its ionization current was only of the order of 10^{-10} ampere due to the low density of air (1.293 Kg/m^3). Therefore, a long measurement time of the ionization current was required to obtain an acceptable image. This corresponded to an approximate dose delivery of 400 millirad from a cobalt-60 source, per measurement at the surface of the detector.

To obtain a higher radiation absorption, thereby increasing signal strength, liquid iso-octane (2-2-4-trimethyl pentane) was evaluated as the ionizing medium. The density of isooctane is 0.69×10^3 Kg/m^3, which is approximately 500 times higher than that of air. It has a resistivity of the order of 10^{17} ohm-cm. This liquid has been used by several other researchers (Wickman 1974, Chu et al. 1980, Johansson and Svensson 1982) for radiation dosimetry and (Meertens et al. 1985) for imaging experiments.

The potential for increased signal strength from an iso-octane filled chamber makes it an attractive ionizing medium. However, it was necessary to verify that its response characteristics, such as rise and decay times, also make it an acceptable ionizing detector. Liquids in

general have a lower charge mobility. It therefore requires more time to collect the charge liberated. If all the charges are not collected prior to the initiation of the next measurement, the leftover charges produce an "after-glow" effect. Therefore the characteristics for both air and iso-octane filled chambers were studied.

Chamber characteristics

Ionization detectors generally exhibit a charge collection efficiency of less than 100% due to ion recombinations. The magnitude of the recombinations is inversely related to the applied collecting voltage and proportional to the distance between the electrodes (Boag 1966). It is expected that the signal from the ion chamber would exhibit a nonlinear behavior.

To observe the deviations from linearity the detector signals were measured at various applied voltages. Figure 4-3 shows the current vs. voltage (I-V) curve for the air filled chamber and figures 4-4a and 4-4b show the I-V curves of the iso-octane filled ion chamber with an electrode separation of 2 mm and 6 mm, respectively. It is apparent from these curves that with air the saturation value of ionization current is approached, while with iso-octane the current is much below saturation, which implies that the ion collection efficiency of the iso-octane filled chambers are much lower than that of the air-filled chamber.

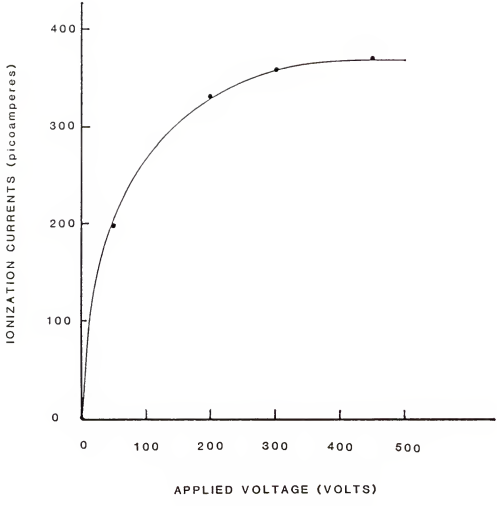

Figure 4-3. Current vs. voltage for the air filled ionization chamber.

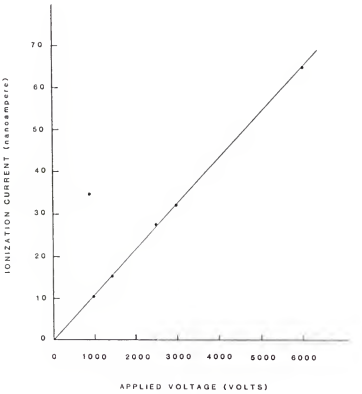

(a)

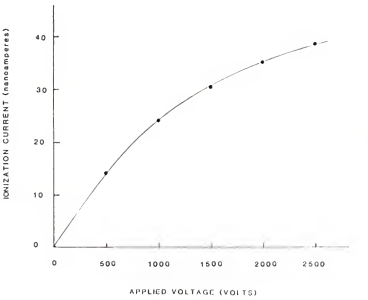

(b)

Figure 4-4. Current vs. voltage for the iso-octane filled ionization chamber: (a) electrode separation distance 6 mm, (b) electrode separation distance 2 mm.

The I-V curve of the iso-octane filled chamber with 6 mm electrode separation shows a linear behavior up to a field strength of 1 kV/mm, showing much lower collection efficiency than the 2 mm separation chamber with the same field strengths. This is due to increased recombination over a longer distance. However, the signal of the iso-octane filled chamber with an electrode separation of 2 mm and with an electric field strength of 1 kV/mm was found to be approximately 100 times higher than the saturation value of the same chamber filled with air.

In the case of a liquid the ion pairs are created very close to each other generating high charge density and as such there is a significant amount of recombination. Also, the rate of charge generation in the ionizing medium is proportional to the absorbed dose rate. It was therefore important to investigate the collection efficiency as a function of dose rate. Relative collection efficiencies for different dose rates were estimated by two methods. In one method the Jaffe (Chu et al. 1980) formulation for saturation current was utilized. The formulation leads to

$$1/i=(1/I)[1+S(1/V)] \qquad (4.1)$$

where i is the collected current, I is the saturation current, E is the electric field and S is a constant. The theory thus predicts a linear relationship between 1/i and 1/V.

Measurements were made to obtain current vs. voltage data with various dose rates. From these data both 1/i and 1/V were determined and were plotted. The value of 1/I was then determined by extrapolation and hence collection efficency was estimated. Although the collection efficiency determined by this method overestimates the actual value (Chu et al. 1980), a relative estimation of collection efficiency was sufficient. Figure 4-5 shows the Jaffe plots of the 2 mm separation chamber for different dose rates. From these plots, a collection efficiency of approximately 50% was estimated for dose rates of 78, 96, and 120 rad/min. This value of the collection efficiency was estimated for a field strength of 1 kV/mm.

The relative collection efficiencies of the 2 mm separation chamber with a field strength of 1 kV/mm were also determined by taking the ratio of the ionization current value of the liquid chamber and the exposure value of a monitoring ion chamber under identical conditions. The monitoring ion chamber was an air ion chamber and the collection efficiency of which was assumed to be constant over the measured range of dose rates. Table 1 shows the measured values and the ratios of readings at different dose rates. This method also suggested that the collection efficiency of the chamber was independent of dose rate at these levels of dose rates. These results agree with the results reported by Chu et al. (1980).

Table 1. Estimation of collection efficiencies of the strip ion chamber as a function of dose rates.

Dose rate (rad/min)	Strip ion chamber reading (nA)	Monitor ion chamber reading (R/min)	Ratio (nA)(min)/R
121	53.5	168.8	0.317
107	46.4	149.6	0.310
96	42.1	133.6	0.315
78	34.8	108.6	0.320
64	28.31	88.9	0.318

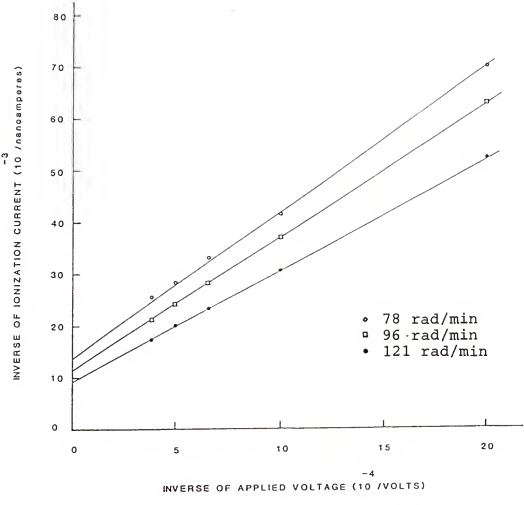

Figure 4-5. Jaffe plot for the iso-octane filled chamber with 2 mm separation between electrodes.

Jaffe's method also suggested that the collection efficiency of the iso-octane chamber with a 2 mm electrode separation distance is approximately an order of magnitude higher than that with a 6 mm electrode separation for equal field strengths. As mentioned earlier, this is due to increased recombination as the ions are drifting through a longer distance.

To obtain the projection data for a real-time imaging device, the complete projection data must be collected in a few seconds, and thus each measurement must be made in a few milliseconds. Moreover, the detector should not exhibit excessive afterglow such that the measurement value at any position of the detector will be affected by the charge produced by the radiation in the previous position. To study these aspects of the detector behavior, the rise and decay times of the ionization current from the detector were measured with a 250 kV x-ray source. For this purpose the chamber was exposed to a series of step inputs of x-ray beam created by a specially designed beam chopper.

The beam chopper was a 40 cm diameter acrylic circular plate of 3 mm thickness with two 90 degree pie-wedge shaped 3.5 mm thick lead sheets cemented at opposite quadrants. The strip ion chamber was positioned radially below the beam chopper and the chopper was rotated by an electric motor with uniform angular speed. When the radiation from the x-ray source is incident on the chamber the rotating beam

chopper creates a series of step inputs to the chamber. The ionization current from the chamber was measured by an electrometer amplifier.

Figures 4-6 and 4-7 show the oscilloscope traces for the output of both air and liquid chambers at different applied voltages. As expected the air chamber showed a very rapid response compared with the iso-octane chambers. For iso-octane chambers the response times were found to have decreased with increased field strengths and with decreased electrode separation distance. This was expected as the total collection time is proportional to the electrode separation distance and proportional to the ion drift velocity. Figures 4-8 and 4-9 show the rise and decay times as a function of applied field strengths for 2 mm and 6 mm electrode separation, respectively, where the rise and decay times are estimated from the time taken by the signal to rise and decay between 10% and 90% of the maximum signal level.

The signal-to-background ratio of the transmitted radiation through the beam chopper with the 250 kV X-ray beam was 25:1. It was estimated that while imaging a typical patient anatomy with a high-energy therapy beam a signal-to-background ratio would be close to unity. Thus, according to the results of figure 4-8, with a field strength of 1 kV/mm a typical rise time and decay time of signals would be 2 to 3 milliseconds for a megavoltage imaging situation. To verify that these rise times and decay

Figure 4-6. Oscilloscope traces for the ion chamber with 2 mm separation: (upper left) air 500 V, (upper right) iso-octane 500 V, (middle left) iso-octane 1000 V, (middle right) iso-octane 1500 V, (bottom) iso-octane 2000 V.

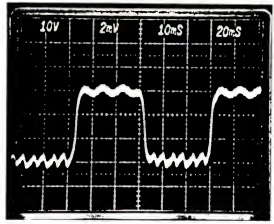
10V
2mV
10mS
20mS

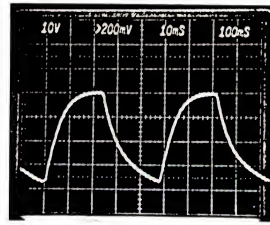
10V
>200mV
10mS
100mS

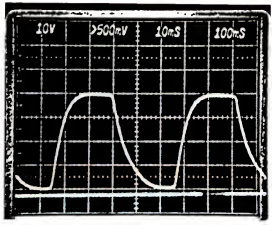
10V
>500mV
10mS
100mS

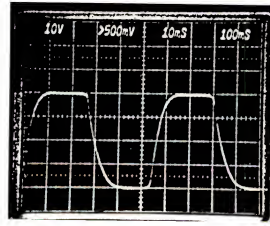
10V
>500mV
10mS
100mS

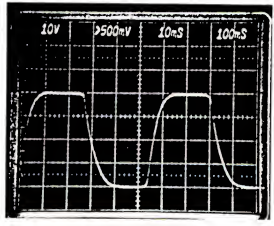
10V
>500mV
10mS
100mS

Figure 4-7. Oscilloscope traces for the iso-octane filled ion chamber with 6 mm separation: (upper left) 1000 V, (upper right) 1500 V, (middle left) 2000 V, (middle right) 3000 V, (bottom) 6000 V.

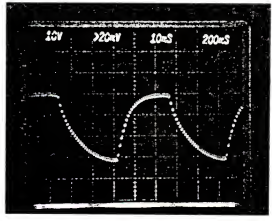
1CV
>20mV
10mS
200mS

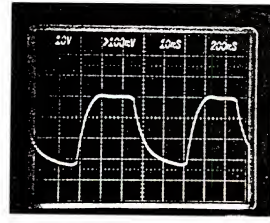
1CV
>100mV
10mS
200mS

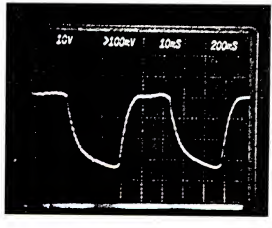
1CV
>100mV
10mS
200mS

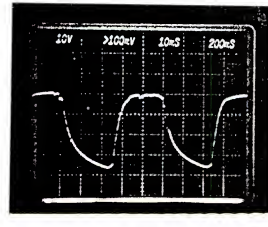
1CV
>100mV
10mS
200mS

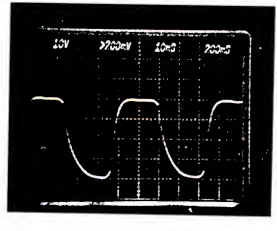
1CV
>200mV
10mS
200mS

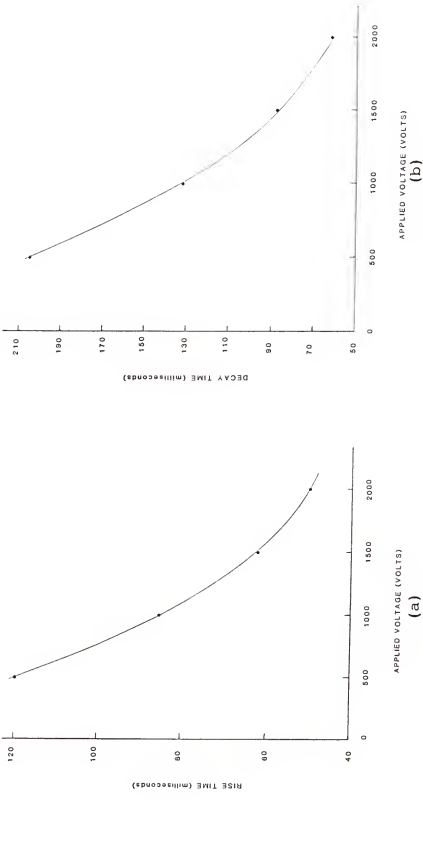

Figure 4-8. Response time as a function of collecting voltage of iso-octane filled chamber with 2 mm separation between electrodes: (a) rise time, (b) decay time.

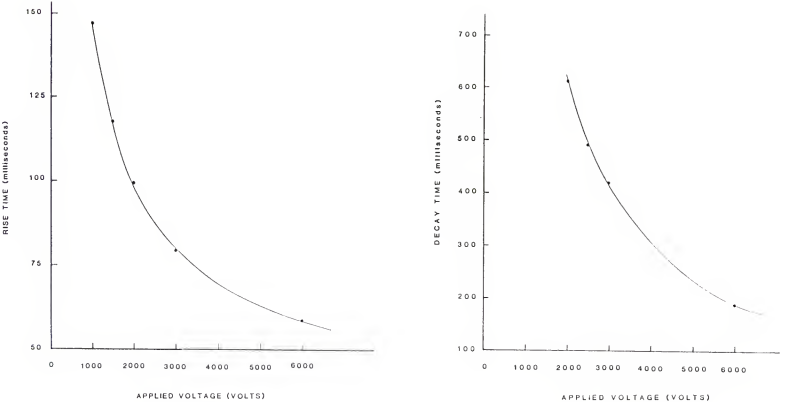

Figure 4-9. Response time as a function of collecting voltage of iso-octane filled chamber with 6 mm separation between electrodes: (a) rise time, (b) decay time.

times of iso-octane are acceptable for megavoltage imaging, two different interfaces were scanned forward and backward with the iso-octane chamber. One of the interfaces consisted of an open radiation field and a lead brick of 3 cm thickness (transmission ratio 7:1) and the other interface consisted of an open radiation field and a 2 cm slab of bone equivalent material (transmission ratio 1.2:1). The scanning was performed by taking measurements in 2 mm steps. Measurement at each position was made by integrating the ionization current for a period of 10 milliseconds. Time spent by the stepping motor to step between successive positions was the time interval between measurements; which was approximately 600 milliseconds. The integration time of 10 milliseconds was chosen because a time of approximately the same amount was estimated to obtain optimum statistics for imaging with the cobalt-60 source as will be discussed in a later section.

Figure 4-10a and 4-10b show the plots of the measured values across the interfaces and show a good agreement (maximum discrepancy of 0.7% for the lead brick and 0.1% for the bone slab) between the values obtained during the forward and backward scanning. This shows that the time-response characteristics of iso-octane would be satisfactory for megavoltage imaging with the prototype CAID.

Finally, the uniformity of the detector along the length of the strip was evaluated using a 250 kV radiation

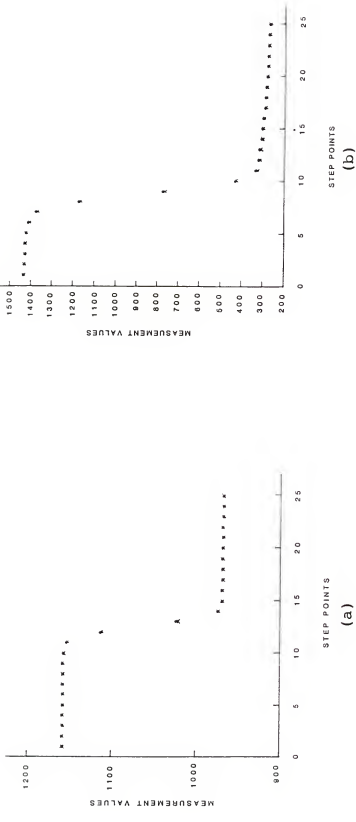

Figure 4-10. Scan values across interfaces: (a) open radiation field-slab of bone equivalent material, (b) open radiation field-lead brick.

source. Ionization currents were measured through a 1 mm aperture. Repeated measurements were made in 2 cm steps along the length of the strip. The measured values, as shown in table 2 were found to be within +/- 1.3% of the average value over a length of 200 mm. The nonuniformity of response was random and is thought to be due to the nonuniformity of the separation distance between the electrode plates.

With the consideration of the above results the iso-octane strip ion chamber was judged to be suitable for imaging experiments. The chamber with the electrode separation of 2 mm was chosen over that with 6 mm separation because of its higher collection efficiency.

Data Acquisition

Perhaps the most important component of the CAID is the data acquisition system. Measurement of a very small ionization current, of the order of a picoampere was required to be made with high accuracy. Also the mechanical movements of the detector were required to be performed with high precision. The repetitive integral measurement technique, described by Fitzgerald (1974), was used to measure the ionization current. This was proved to be an effective technique for measurement of small currents. An electrometer operational amplifier was used for this purpose. Two stepping motors were used for the

Table 2. Uniformity of response along the length of the strip ion chamber.

Position along the length of the strip chamber	Measured current (nanoampere)
1	4.48
2	4.49
3	4.49
4	4.48
5	4.53
6	4.48
7	4.54
8	4.56
9	4.51
10	4.48
11	4.49

translational and rotational movements of the detector. A microcomputer was interfaced with the amplifier network and the motor controller to perform the data acquisition sequence. Figure 4-11 shows a typical timing sequence for a measurement cycle.

At the beginning of each measurement the electrometer was reset to zero volts. Current integration by the amplifier was allowed until the prescribed time interval elapsed at which time the analog-to-digital conversion of the integrated signal was performed. The detector was then moved to the next position by sending pulses to the stepping motor. Thus, a measurement cycle was completed. A description of each of the components follows.

Electrometer amplifier

An operational amplifier (AD 515) with a feedback capacitor as shown in figure 4-12, was used to integrate the current from the ion chamber. The amplifier was a precision, low power field-effect type with an input impedance of 10^{10} ohms and an input bias current of 75 fA. The voltage output of the amplifier at the end of the integrating cycle is proportional to the accumulated charge on the integrating capacitor and is given by

$$V(t) = Q/C = \int Idt/C. \qquad (4.2)$$

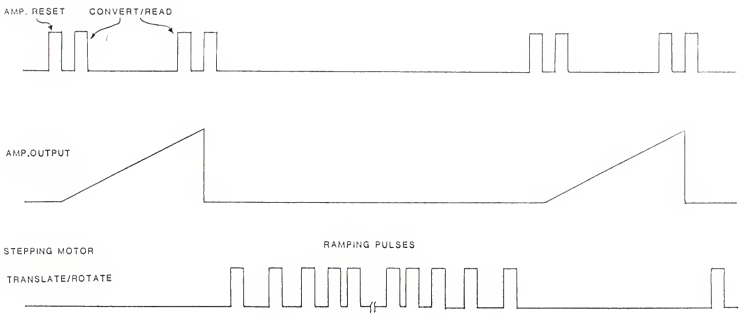

Figure 4-11. Timing sequence of the data acquisition system.

Amplifier reset network

It was necessary to reset the electrometer operational amplifier at the beginning of each measurement. The switching of the integrator to the reset mode was accomplished by utilizing a pair of field-effect-transistors (FET) as shown in figure 4-12. These FETs are normally nonconducting with zero gate voltage and become conducting when a positive voltage is applied to the gate. The integrating capacitor was reset during this conducting phase when the electrometer output was connected to the input through the transistors.

Two transistors were connected in series as a switch to reduce leakage problems. The drain of one transistor was connected to the source of the other and this junction was connected to voltage common over a small resistor keeping the junction point of the two transistors essentially at zero volts during integration. The voltage at the drain of transistor B increased to a maximum of 15 volts during integration. However the cut-off resistance between the drain and the source of these transistors is of the order of 10^9 ohms so the maximum leakage current across transistor B was of the order of 10^{-8} amperes which had an insignificant effect on the output of the amplifier. If just one transistor were used the full 15 volts developed at the output would be the voltage across the source and the drain and the potential of leakage to the input would be great.

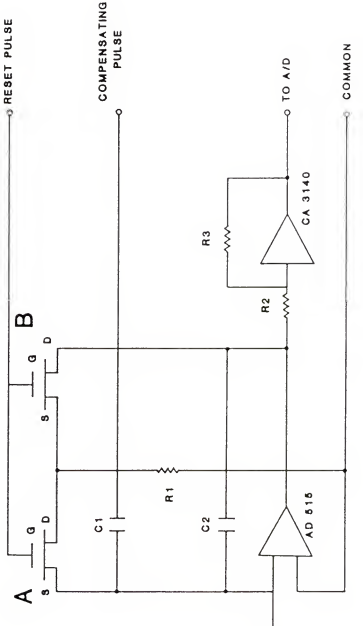

Figure 4-12. Repetitive integral electrometer amplifier circuit.

Another potential problem of using just one transistor was the capacity between the source and the drain. This capacity is in parallel with the integrating capacitor.

The two-FET resetting network was theoretically all that was needed to accomplish the reset of the integrating capacitor. A problem however did exist when the transistors turned off. The transistors ceased to conduct at some positive voltage above zero volts but the reset pulse at the gate went entirely to zero volts. The capacity between the source and gate of transistor A became important after the transistor ceased to conduct, when the integrating capacitor began to charge. The capacity between the source and gate of transistor A could cause charges to transfer to the input during the time after the transistor had ceased to conduct and before the gate voltage reached zero. This transfer of charge caused an immediate change in the output of the amplifier. This problem was overcome by inserting a compensating pulse at the input of the amplifier. The compensating pulse was of opposite polarity to that of the reset pulse.

The reset and compensating pulses were generated by an assembly of dual monostable multivibrators (CD 4098) as shown in figure 4-13a. Computer pulses were used to trigger the multivibrators whose pulse widths were determined by selecting values of resistors and capacitors in the circuit. The timing diagram of the reset and compensating pulses is shown in figure 4-13b.

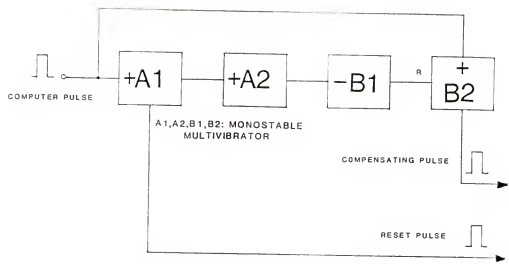

(a)

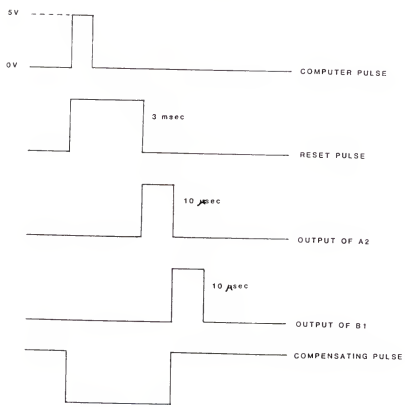

(b)

Figure 4-13. Amplifier reset diagram: (a) reset network, (b) pulse timing.

Analog-to-digital-converter

The output of the electrometer amplifier was passed to a 12-bit ADC (AD 574). The ADC was of the successive approximation type with a 3-state output buffer circuitry, which allowed direct interface to a microprocessor bus. The ADC had a bus access time of 250 nanoseconds and a conversion time of 25 microseconds. The input voltage range of 0 to +10 volts was used. Computer pulses were used to control the operations of the ADC. Decoupling capacitors were used with the power supplies to reduce noise.

Stepping motors

Mathematical reconstruction of the image with minimal artifacts requires high precision in geometrical accuracy of translational and rotational motions of the strip detector. Two identical stepping motors with their controllers interfaced with the microcomputer were used for uniform translational and rotational movements of the ion chamber. The step angle of the motors was 1.8 degrees and a maximium speed of up to 3000 steps per second was provided by the controller. For translational motion of the detector a ball screw with a lead of 5 mm was connected to the stepping motor. To reduce backlash two ball nuts were backloaded. A worm gear was used for the rotational motion. Software pulse ramping sequences were used for acceleration and deceleration of the motors.

Computer/software

The overall coordination and functions of the amplifier network, the ADC and the stepping motors were controlled by the microcomputer. A software package, utilizing a combination of BASIC and assembly language programs was developed for the data acquisition system.

The input parameters required by the software were the time interval of signal integration, the number of translational steps and the number of angular views. The number of angular views (m) was chosen to be $m = \pi n/4$, where n is the number of translational steps. This number of angular views was determined to be sufficient to produce images with negligible artifact (Urie 1979).

At the beginning of each integration a pulse was sent from the computer to trigger the multivibrator circuitry which generated pulses to reset the electrometer amplifier to zero volts. After reset the amplifier began integration. A prescribed integrating time interval was determined by count down loops. As soon as the time interval had elapsed analog-to-digital conversion was initiated by sending appropriate pulses to the ADC. At the end of the conversion cycle the 12-bit data output was read as two 8-bit bytes (one with 8 data bits, the other with 4 data bits and 4 zeros). To eliminate the uncertainties of zero level reset of the amplifier, two measurements were made at each position of the detector one near the beginning and the

other at the end of the integrating cycle. The difference of the readings was the net value for the desired time interval.

After the data were collected at one position, the detector strip was moved to the next translational position by sending pulses to the translational motor. Again the sequence of reset, integration, analog-to-digital conversion and data storage took place. This process of data collection and translation was repeated until the detector stepped across the desired field of view. After completion of a view the detector was rotated to the next angular setting by sending pulses to the rotational motor. Again a series of data collection and translational movements took place to complete the view. In this way the imaging field was scanned for the prescribed number of views. Finally, all the data were written to a floppy disk.

Precise positioning of the detector at the outset of the scan was important because the rotational center of the scanner must correspond to the center assumed by the reconstruction algorithm.

Reconstruction and Display

The images were reconstructed from the projection data by a convolution filtered back projection algorithm (Ramachandran and Laksminaryanan 1971). A detailed discussion of the reconstruction algorithm is given in Appendix A.

The reconstruction of the image was performed with a PDP-1134 computer. Finally, the reconstructed image was mapped to a digital image of range between 0 to 255 by linear scale and displayed on the monitor by utilizing an 8-bit deep frame grabber (Model 274C Colorado video).

System Performance and Results

System Noise

The system noise was estimated from the standard deviation (Leong 1984) of the integrated signal with the strip chamber in a stationary position in an open radiation field. The SNR for the air chamber system was estimated to be 2200:1 for an integration time of 300 milliseconds (400 millirad), and for the liquid system it was 2500:1 for an integration time of 20 milliseconds (25 millirad). For the imaging experiment the integration time for each measurement was appoximately 300 milliseconds for air and 20 milliseconds for the liquid system, respectively.

To approximate the contribution of the photon statistics to the overall noise the number of photons incident on the ion chamber was estimated. For an exposure of 20 milliseconds this number was estimated to be of the order of 10^8 and thus the SNR due to photon statistics only would be of the order of 10^4. It is therefore concluded that the system noise was not photon limited but was mainly composed of electronic noise.

Spatial Resolution

The spatial resolution of the reconstructed image is determined by the combined effect of the detector resolution and reconstruction resolution (Tanaka and Iinuma 1975). During the projection data collection, the profile distributions are convolved with the detector point spread-function (PSF) and these data are in turn convolved with the reconstruction PSF which corresponds to the Fourier transform of the window function of the reconstruction filter. The ramp filter cancels out the (1/r) blurring function of the back-projection process.

The system resolution of an image can be approximated by

$$R_s^2 = R_d^2 + R_r^2 \qquad (4.3)$$

where R_s, R_d, R_r are the respective system, detector and reconstruction resolution (full-width at half-maximum of PSF).

The reconstruction resolution corresponding to the ramp filter was set equal to the sampling interval (Lim et al. 1982). The PSFs for the iso-octane filled chamber were determined from the edge response function (ERF) data (method is discussed in Appendix B). The detector system resolution was determined to be 4.0 mm, for a sampling interval of 1.98 mm, which was in good agreement with the prediction of the sampling theorem (Bracewell 1965). The

system resolution was determined from the reconstructed image of an edge and was found to be 4.2 mm. Figures 4-14 and 4-15 show the ERFs and corresponding PSFs for the detector and system resolution, respectively. The result agreed well with the approximate relationship given by equation (4.3), which yields 4.46 mm as the system resolution.

Contrast Resolution

Since the poor contrast of portal images was the primary concern of this work, a low contrast phantom made of 4 cm thick bone equivalent material with holes of different sizes and depths was used for contrast evaluation of images. Figure 4-16 shows the schematics of the low contrast phantom with different hole sizes, depths and their corresponding contrast values. The reconstructed images of the phantom were compared with the image of the port film. Besides visual evaluation, comparison between the port film image and the reconstructed image was performed by comparing the image contrast C_i, given by

$$C_i = |I_o - I_b| / I_b$$

where I_o and I_b are the pixel values of the object and the background respectively. Image contrast of an identical image position is calculated for both the film image and the reconstructed image where the values of I_o and I_b were estimated by taking an average of 3x3 pixels area of the

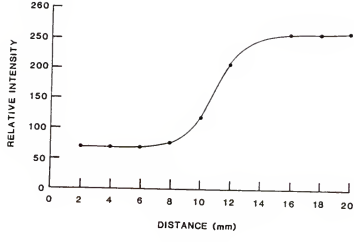

(a)

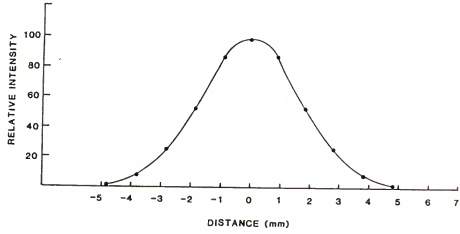

(b)

Figure 4-14. Detector spatial resolution:
(a) ERF, (b) PSF.

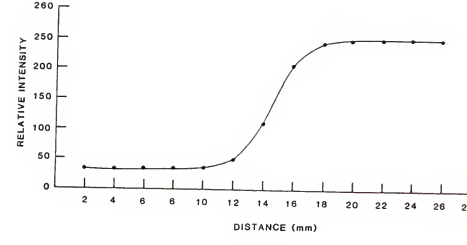

(a)

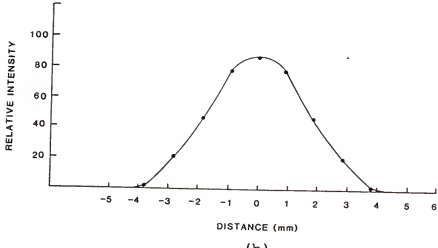

(b)

Figure 4-15. System spatial resolution:
(a) ERF, (b) PSF.

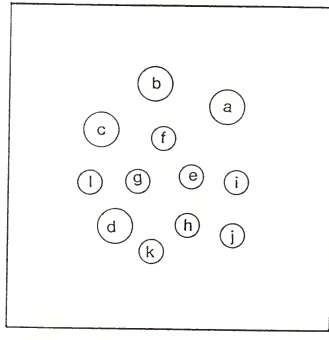

Position	Diameter(mm)	Hole depth(mm)	%Contrast
a	6.0	20.0	18.0
b	6.0	17.0	15.0
c	6.0	12.0	11.2
d	6.0	8.5	8.1
e	4.0	20.0	18.0
f	4.0	11.8	11.0
g	4.0	10.0	9.4
h	4.0	7.0	6.7
i	4.0	4.0	3.9
j	4.0	3.5	3.4
k	4.0	2.5	2.4
l	4.0	1.4	1.3

Figure 4-16. Low contrast phantom, 4 cm thick bone equivalent material.

object in question and the background, respectively. This comparison was possible with the low contrast phantom only because a well defined object area was identified inside the image of a bigger hole.

Effect of dose-per-measurement on contrast. To determine an optimum dose (integration time) for each measurement which would produce an acceptable image, the low contrast phantom was scanned with various integration times. The corresponding images were reconstructed and compared with the film image. As shown in figure 4-17, reconstructed images with integration of 6 millirad and 12 millirad yielded images of lower contrast resolution than the film image due to their lower SNR values. In these images the number of holes visible is 9, while 11 holes are visible in the film image. The image with 19 millirad yielded an image of equal contrast resolution to that of the film image. Image with 25 millirad appears to have a higher contrast resolution than the film image as shown in the figure, where the shallowest hole is visible in the reconstructed images but not visible in the film image. The shallowest hole has a contrast of 1.3%, where contrast is defined by

$$C=|I_1-I_2|/I_2.$$

I_1 and I_2 are the transmitted radiation intensities through the background and the object in question, respectively.

Figure 4-17. Images of the low contrast phantom: (upper left, upper right, middle left, and middle right) CAID images with integration per measurement of 6, 12, 19, and 25 millirad, respectively, (bottom) film image.

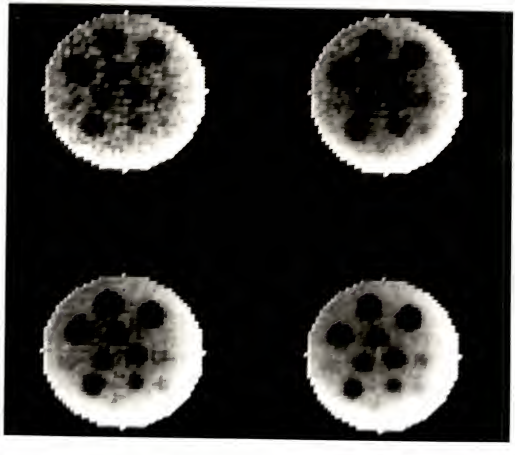

The image contrast of the hole in the port film image, labeled b in figure 4-16, was found to be 0.17. For the same hole the image contrast of the reconstructed image (with 25 millirad) the image contrast was 0.80.

Effect of scatter rejection by scatter-shield on contrast. The effect of scatter on contrast resolution is well known. It was therefore interesting to evaluate the presence of scattered signal in projection data obtained by the strip chamber.

The CAID has some inherent scatter rejection mechanism due to the one-dimensional geometry of its strip detector. This feature, and the 6 mm thick acrylic plate, which was glued on to the front surface of the detector for structural stability, act to prevent low energy scattered photons from entering the sensitive volume of the detector. A further attempt was made to evaluate and minimize the scatter to primary ratio (S/P) by using a lead scatter-shield on the surface of the detector. The values of S/P were estimated by a similar method as was used for the fluoro system.

A uniform 10 cm thick water equivalent material was used to provide the scatter. The integrated signals from the detector were measured with a field size of 20 cm along the length of the detector and various widths perpendicular to the detector length. The plots of the integrated signal values vs. field widths were generated for different thicknesses of lead on the detector surface. The primary values were estimated by extrapolating the curves to zero

width. Thus the scatter contribution for a typical field size was determined by subtracting the primary value from the primary plus scatter value. The S/P values for various thicknesses of lead are given in table 3; which shows that the S/P values did not improve significantly with the scatter-shield.

To double check the effect of the scatter-shield on the contrast, the low contrast bone phantom was scanned with lead on the surface of the detector and an image was reconstructed. Figure 4-18 compares the phantom image with and without the scatter-shield screen, showing no improvements in contrast. The image contrast of the hole labeled b was determined to be 0.79 and 0.80 in the images with and without scatter shield, respectively.

Effect of background-scatter subtraction on contrast. The effect of scatter can be partially corrected in software by subtracting a uniform background of scatter radiation (Peschmann 1981). Figure 4-19 shows the effect of different levels of subtraction on the reconstructed images of low contrast bone phantom. It can be seen from the images that the image contrast improves with increasing level of background subtraction but excessive amounts of subtraction causes lowering of the intensity values predominantly to the center of the image. However, an optimum level of background was determined to be approximately equal to the measured value when the detector was just outside the radiation field. The same effects of background subtraction

Table 3. Estimated values of scatter-to-primary ratio at various thicknesses of scatter-shield.

Thickness of lead placed on the detector surface (mm)	Estimated scatter to primary ratio (S/P).
2.0	0.277
4.0	0.270
6.0	0.265
8.0	0.262

Figure 4-18. Effect of scatter shield on low contrast phantom images: (top) without scatter shield, (bottom) with scatter shield.

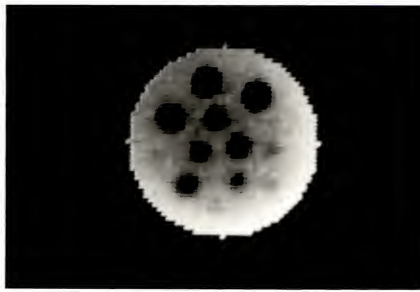

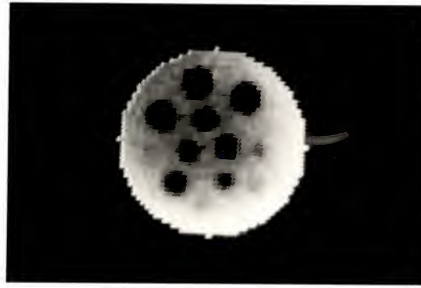

Figure 4-19. Effect of background subtaction by different levels before reconstruction: (upper left) no subtraction, (upper right) subtraction of 400, (lower left) subtraction of 800, (lower right) subtraction of 1000. Where the measured value just outside the radiation field was 850.

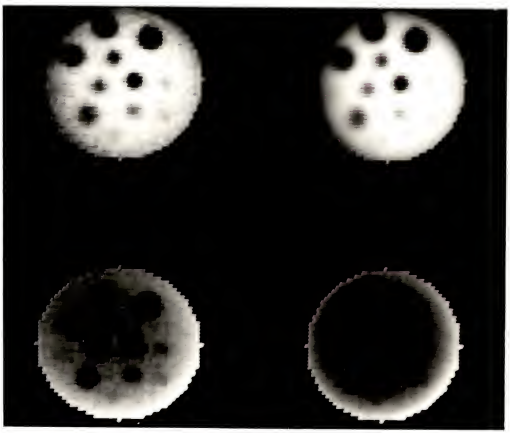

on reconstruction were also verified with other clinically interesting images.

From the above consideration it was decided to use a dose of approximately 25 millirad per measurement with the iso-octane chamber. The scatter shield was not used on the surface of the detector as it did not improve the image contrast but did reduce the signal strength. The image reconstructions were performed by subtracting a background level determined from the measured value with the detector positioned just outside the radiation field.

Images

The images of the low contrast phantom descussed above and the images to be discussed in the following were obtained with a cobalt-60 source.

As suggested by Joseph (1981) the geometrical alignment of the scanner was checked by imaging a test phantom. The test phantom was a gear wheel with a central rod and six non central circular holes. Figure 4-20 is the image of the test phantom, obtained with the iso-octane filled chamber, showing no misalignment artifact. Images of various test phantoms were obtained with the prototype CAID and compared with corresponding film images. Of these, only clinically interesting images will be discussed.

A human head phantom consisting of a skull encased in a tissue equivalent material and a cow vertebrae embedded in

Figure 4-20. Image of a gear-wheel showing no misalignment artifact.

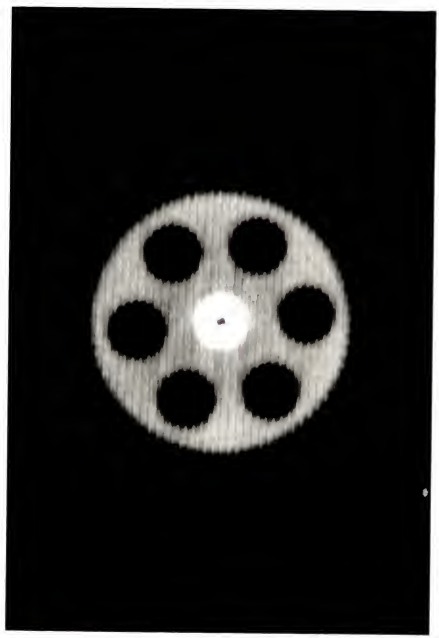

5 cm wax were imaged with the air chamber and the iso-octane chamber and were compared with the corresponding film images. As shown in figures 4-21 and 4-22, the air chamber images have similar contrast to that of the film images. The iso-octane chamber images are of higher contrast than the unenhanced film images. The slight unsharpness of the air chamber images is due to the longer range of electrons in air causing increased cross over of electrons between the charge collecting volume and adjacent volumes. The longer range of electrons in air compared to iso-octane can be understood from the estimated values of corresponding stopping powers. Considering the equivalent Z value of iso-octane the stopping power was estimated to be 1.17 MeV/cm; whereas the stopping power of air is 2.71 keV/cm (Johns and Cunningham 1983). The air chamber was ultimately judged to be inadequate due to its very low signal strength and therefore all the subsequent imaging experiments were performed with the iso-octane chamber. Also shown in figure 4-22 is the image of the cow vertebrae obtained with the plastic scintillator.

Figures 4-23 and 4-24 show the CAID and film images of the anterior-posterior (AP) and lateral views of a human cadaver head respectively. In the AP view of the CAID image the air-tissue-bone interfaces are seen more clearly than the film image allowing better visualization of the nasal cavity, maxillary sinuses and frontal sinus. In the lateral view also the CAID image is sharper and of better contrast

Figure 4-21. Images of a human head phantom: (upper left) port film, (upper right) CAID with air filled chamber), (lower left) CAID with iso-octane filled chamber, (lower right) edge enhanced image with the iso-octane chamber.

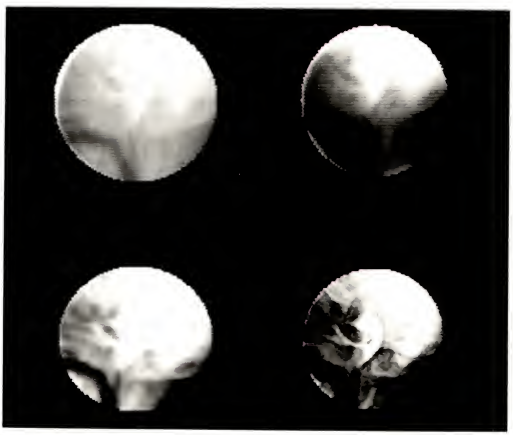

Figure 4-22. Images of the cow vertebrae: (upper left) film, (upper right) CAID with air filled chamber, (lower left) CAID with iso-octane filled chamber, (lower right) CAID with plastic scintillator.

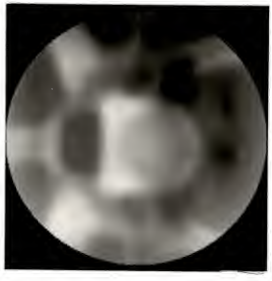

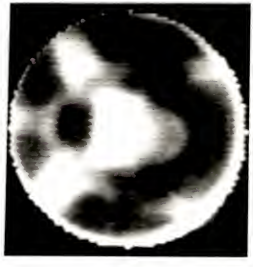

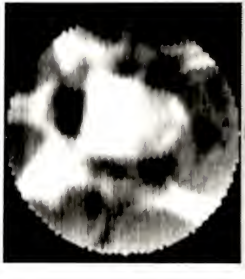

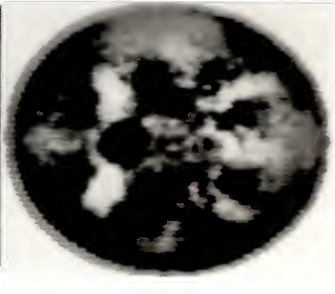

Figure 4-23. AP view of a human cadaver head: (upper left) film, (upper right) CAID image, (middle left) enhancement of CAID image by linear contrast enhancement, (middle right) edge enhancement of the image of the middle left, (lower left) AHE on the CAID image, (lower right) edge enhancement of the image of the lower left.

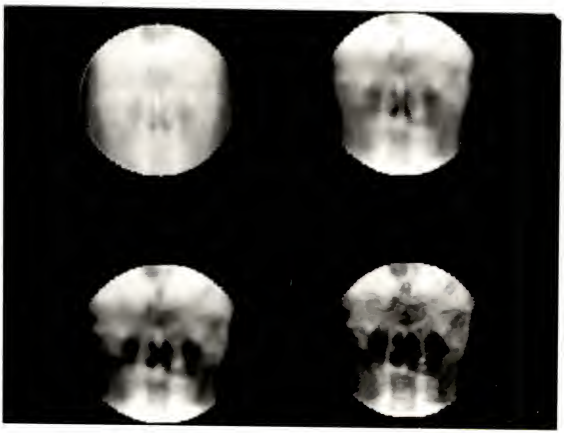

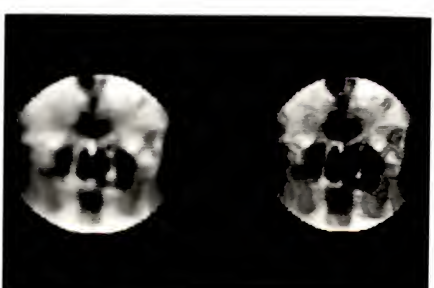

Figure 4-24. Lateral view of a human cadaver head: upper left) film, (upper right) CAID image, (middle left) enhancement of CAID image by linear contrast enhancement, (middle right) edge enhancement of the image of the middle left, (lower left) AHE on the CAID image, (lower right) edge enhancement of the image of the lower left.

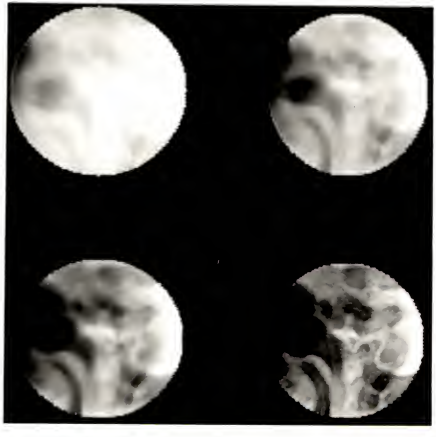

than the film image and thus allows better visualization of the base of skull, base of tongue, nasopharynx and soft palate.

Finally, an attempt was made to demonstrate the imaging ability of this system with the pulsed radiation produced by a linear accelerator (Linac) as opposed to continuous radiation of a cobalt source. The signal integration from a Linac source cannot be consistently performed by simply specifying a time interval as was possible with a cobalt source. This is due to the fact that within a specified time interval the number of pulses delivered from the Linac may not be constant. A typical pulse output rate from the Linac is 320 pulses per second, where the length of each pulse is 4 microseconds and therefore the interval between pulses is approximately 3 milliseconds. Thus for a typical integration time of 10 milliseconds the number of pulse count could be ranging from three pulses to four pulses. Any fraction of the first or the fourth pulse may also be counted depending upon the intiation time of integration. To account for this inconsistency in the number of pulses, a reference chamber was used for dose normalization.

The measurement values of the strip ion chamber were normalized with respect to the reference chamber positioned above the imaging phantom. The normalization allowed the measurements for a specified time interval irrespective of the number of pulses and dose delivered per pulse. The data acquisition system was modified to incorporate an identical

electrometer amplifier and ADC to monitor the reference chamber. The reference ionization chamber was a 2 cm diameter circular parallel plate chamber with 2 mm separation between the high voltage electrode and the collecting electrode. Iso-octane was used as the ionizing medium and a field strength of 1 kV/mm was used to provide the same response as that of the measuring chamber. Resetting of both the amplifiers and triggering of both the ADCs were performed at the same instant.

The low-contrast bone material phantom was imaged with 8 MV x ray produced by a Philips SL75-20 Linac. The image was found to be excessively noisy. The noisy image resulted from the radio-frequency noise picked up by the unshielded cables of the data acquisition system. It was therefore concluded that the present system with its unshielded cables would not be suitable for data acquisition in the high radio-frequency field produced by a Linac. Further imaging experiments were not performed with a Linac.

Enhanced Images

Since the CAID images are in digital form, some simple image enhancement algorithms can be easily incorporated into the data processing system. Various image enhancement techniques, as described in Chapter V were applied to the CAID images. A combination of smoothing by median filter, contrast enhancement by linear transfer function with clipping or AHE followed by edge enhancement

seems to yield images of very high quality. Examples of processed images, which are produced by smoothing, contrast enhancement followed by edge detection with a threshold gray level of ten are shown in figures 4-21, 4-23 and 4-24. The enhanced images show a much better discrimination between tissue, bone and air passages and thus allow easier visualization of the major anatomical landmarks.

Discussion

The major goal of this work was to answer two key questions: whether it is feasible to generate digital portal images by the Coded Aperture Imaging Device with similar contrast to those of film images and whether the system can be used as a real-time imager.

It was demonstrated that the images produced by the CAID in association with image enhancement techniques are of higher contrast than those of the metal screen film images.

The data acquisition time for clinically interesting images was typically 20 milliseconds per measurement. For 100 translations and 80 projections the net data measurement time was approximately 160 seconds. But a total data acquisition time of about 80 minutes was required including the translational and rotational movements. A practical device however, will have multiple strip chambers requiring no translational motion and could collect data by rotational motion only in a much shorter time. For instance, for a

field of view of 40 cm in diameter, 200 detector channels could be employed, requiring 160 projections for a suitable image. Thus, a net data collection time would be 3.2 seconds. With a faster stepping motor the rotational movement can be accomplished in a few seconds. The image reconstruction also can be performed with a faster computer in 2 to 3 seconds. Therefore, it is expected that a large portal image can be generated in 5 to 10 seconds. Of course, a smaller portal image can be generated in an even shorter time.

From the above discussion it is evident that the CAID cannot produce an image in real-time in the usual sense. Real-time imaging implies the generation of images in video-frame rate; 30 frames per second. However, for localization and verification of radiation therapy beam, images produced in 5 to 10 second intervals would be quite satisfactory.

The system spatial resolution is dependent upon the sampling frequency of data collection. Since the setup and localization errors in radiation therapy are considered to be 5 mm or greater, a spatial resolution of approximately 4 mm was thought to be sufficient for portal imaging. It was demonstrated that the system spatial resolution was adequate for viewing interesting anatomical structures. In the event a higher spatial resolution is needed the sampling frequency of the device could be increased at the cost of more computing resources and data acquisition time.

CHAPTER V
IMAGE PROCESSING

Whenever a picture is converted from one form to another, e.g., imaged, copied, scanned, transmitted, or displayed, the "quality" of the output picture may be altered from that of the input. Image processing techniques attempt to improve the "quality" of the image. For the purpose of the present investigations, contrast and edge enhancement aspects of image processing were considered.

Image enhancement processes consist of a collection of techniques that seek to improve the visual appearance of the image, or to convert the image to a form better suited to human or automated machine analysis. There is no unifying theory of image enhancement at present, because there is no general standard of image quality that can serve as a design criteria for an image enhancement processor.

Enhancement methods may be divided into two broad categories, methods in frequency domain and methods in spatial domain. Processing techniques in the first category are based on the Fourier transform of an image. The spatial domain on the other hand, refers to the image plane itself and approaches in this category are based on direct manipulation of the pixels in the image.

The foundation of the frequency domain techniques is the convolution theorem. Let g(x,y) be an image formed by the convolution of an image f(x,y) and a position invariant operator h(x,y), that is

$$g(x,y)=h(x,y)*f(x,y). \tag{5.1}$$

Then using the convolution theorem the frequency domain relation becomes

$$G(u,v)=H(u,v)F(u,v) \tag{5.2}$$

where G(u,v), H(u,v), and F(u,v) are two-dimensional Fourier transforms of g(x,y), h(x,y) and f(x,y), respectively. In a typical image enhancement problem f(x,y) is given and the goal, after computation of F(u,v), is to select H(u,v) so that the desired image, given by

$$g(x,y)= F^{-1}[H(u,v)F(u,v)] \tag{5.3}$$

where F^{-1} represents the two dimensional inverse Fourier tranform exhibits some highlighted feature of f(x,y). For instance, edges in f(x,y) can be accentuated by using a high-pass frequency filter and f(x,y) can be smoothed by a low-pass filter. Multiplication of F(u,v) by H(u,v) is a filter operation.

The spatial domain techniques of image processing are based on gray level mappings, where the type of mapping used depends on the criterion chosen for enhancement.

The spatial domain processes are often easy to implement, and in this domain edge sharpening, smoothing, contrast manipulation and various kinds of local and nonlocal averaging techniques can be employed. Algorithms for various enhancement techiques in spatial domain were developed and applied to images. A brief discussion of some of the interesting techniques follows.

Preprocessing

Frame Averaging

In the case of the Fluoro system, single frame images are found to be statistically noisy. The statistical nature of the radiation output, absorption of radiation by screen phosphors and electronic noise introduced by the camera and the digitizer contribute to salt and pepper noise. To improve the image statistics, an average of multiple frames is taken. The mathematical basis of noise reduction by averaging can be understood according to the following. Consider a noisy image g(x,y) which is formed by the addition of noise n(x,y) to an original image f(x,y) that is

$$g(x,y)=f(x,y)+n(x,y). \qquad (5.4)$$

If the noise is uncorrelated and has zero average value and if an image g(x,y) is formed by averaging M different noisy images

$$\bar{g}(x,y) = \frac{1}{M} \sum_{i=1}^{M} g(x,y). \qquad (5.5)$$

Then it follows that (Papoulis 1965)

$$E\{\bar{g}(x,y)\} = f(x,y) \qquad (5.6)$$

and

$$\sigma^2_{\bar{g}}(x,y) = \frac{1}{M} \sigma^2_n(x,y) \qquad (5.7)$$

where $E\{g(x,y)\}$ is the expected value of $g(x,y)$, $\sigma^2_{\bar{g}}$ and σ^2_n are variances of $g(x,y)$ and $n(x,y)$. Thus the standard deviation at any point in the image is given by

$$\sigma_{\bar{g}}(x,y) = \frac{1}{\sqrt{M}} \sigma_n(x,y). \qquad (5.8)$$

Equations (5.7) and (5.8) indicate that as M increases the variabilty of the pixel value decreases and as the number of noisy images in the averaging process increases $\bar{g}(x,y)$ approaches closer to $f(x,y)$. Examples of noise reduction in images, by averaging multiple frames, has been presented in Chapter III (figure 3-5).

Smoothing

Even after frame averaging, the images contain some salt and pepper noise due to noise in the sampling system or in the transmission channel. This noise could be further reduced by spatial smoothing techniques. Neighborhood averaging given by

$$g(x,y) = \sum_{S} W_{nm} f(n,m) \qquad (5.9)$$

where S is the set of coordinates of points in the neighborhood and W is the weighting factor, is one of the standard methods for image smoothing. Smoothing by nine point weighted averaging given by

$$\begin{aligned} g(x,y) = 1/16[&f(x-1,y-1)+2f(x,y-1)+f(x+1,y-1)+ \\ &2f(x-1,y)+4f(x,y)+2f(x+1,y)+f(x-1,y+1) \\ &+2f(x,y+1)+f(x+1,y+1)] \end{aligned} \qquad (5.10)$$

seems to yield optimum smoothing. Smoothing by averaging technique works well in reducing the salt and pepper noise but at the same time results in blurring of sharp edges present in the image. An alternative to this is median filtering. In this method of smoothing each pixel value is replaced by the median value of pixels in a specified neighborhood. Median filtering preserves edges but requires more computing time.

Contrast Enhancement

The most important goal of the present investigation was to obtain images with improved contrast. Contrast can be manipulated both in linear and nonlinear scales.

Enhancement by Linear Transfer Function

The linear scale contrast manipulation is usually done by stretching the input range of pixel value to the whole

dynamic range available in the display system. This is accomplished by a linear transfer function. A modification of the linear scaling is to clip extreme brightness values of the processed image to some maximum and minimum values (Pratt 1978). Figure 5-1 illustrates the linear transfer functions for contrast enhancement.

Figures 5-2 and 5-3 show an example of unprocessed fluoro image and contrast enhanced image of a human skull with their corresponding gray level histograms. The gray level histogram of such an image that has been linearly scaled is usually highly skewed toward the darker levels. A majority of the pixels have a luminance less than the average. In such images detail in the darker regions is not often perceptible. One means of enhancing these type of images is a technique called histogram modification in which the original image is rescaled so that the histogram of the modified image follows some desired form.

Enhancement by Non-Linear Transfer Function (Histogram Modification)

Foundation

The discussion below follows the development of Gonzalez and Wintz (1977). Let the variables r and s represent the gray levels and $p_r(r)$ and $p_s(s)$ the corresponding probability distributions of the original and enhanced images respectively. Let us also denote T as the

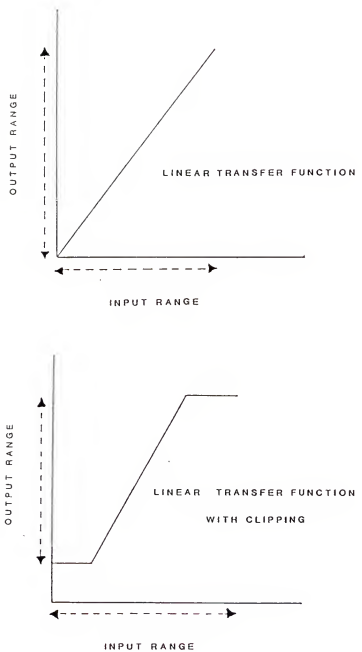

Figure 5-1. Contrast enhancement by linear scaling.

Figure 5-2. Human skull: (top) fluoro image, (bottom) corresponding histogram.

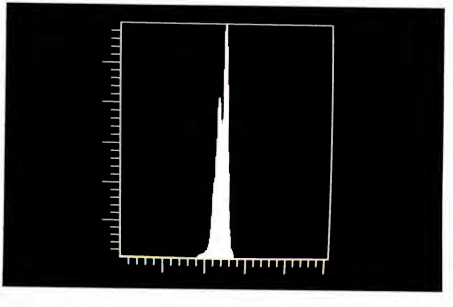

Figure 5-3. Contract enhancement of human skull image by linear scale: (top) enhanced image, (bottom) corresponding histogram.

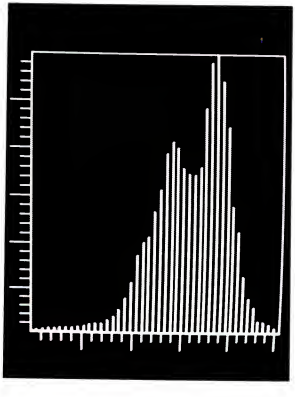

transfer function, which maps input to output gray levels,

$$s=T(r). \tag{5.11}$$

It is assumed that T(r) is single valued and monotonically increasing in the dynamic range of the image. Using elementary probability theory, the probability density function of the transformed gray levels is given by

$$P_s(s)=[P_r(r)\frac{dr}{ds}]_{r=T^{-1}(s)}. \tag{5.12}$$

The following enhancement technique is based on modifying the appearance of an image by controlling the probability density function of its gray levels via the transformation function T(r).

Histogram equalization

Histogram equalization was found to be an effective method of enhancing an image which contained pixels with a narrow range of gray levels (Andrews et al. 1972, Hall 1974). In this method the histogram of the enhanced image is forced to be uniform.

If the output image is to possess uniform histogram, then the probability distribution function $P_s(s)$ should be equal to unity and then integration of equation (5.12) yields

$$s=T(r)=\int_0^r P_r(w)\,dw \tag{5.13}$$

where w is a variable of integration. The right most side

of equation (5.13) is recognized as the cumulative distribution function (CDF) of r. This development indicates that using a transformation function equal to the CDF of r produces an image whose gray levels have a uniform density.

In order to be useful for digital image processing, the concept developed above must be formulated in digital form. For gray levels which assume discrete values, the probability relation is given by

$$p_r(r_k) = n_k/n \qquad 0 \le r_k \le 1 \qquad k=0,1,\ldots,L-1 \qquad (5.14)$$

where L is the number of levels, $p_r(r_k)$ is the probability of the kth gray level, n_k is the number of times this level appears in the image, and n is the total number of pixels in the image. The discrete form of equation (5.12) is given by the relation

$$s_k = T(r_k) = \sum_{j=0}^{k} n_j/n = \sum_{j=0}^{k} p_r(r_j) \qquad (5.15)$$

$$k=0,1,\ldots,L-1 \ .$$

A software for histogram equalization was written and applied to the phantom images. This process enhances the contrast of the image by a gray level assignment scheme, which is based on the image as a whole. Thus contrast

enhancement by this procedure, as illustrated in figure 5-4, does not enhance small detail of the image throughout the field. This is not desirable in the present application. A modification of this method termed as adaptive histogram equalization (AHE) has been developed by Pizer et al. (1984) for application to computerized tomography (CT) images.

Adaptive histogram equalization

The idea of adaptive histogram equalization (AHE) depends upon the fact that if the gray level assignment scheme is to optimize the transmission of information in the pixel values about some image feature, it must depend on the distribution only in a region local to the feature. Thus, the assignment scheme should adapt to the regional distribution of pixel values and also it should vary smoothly across the image.

This objective can be achieved by letting the gray level mapping for each pixel depend directly on the region of a specified size and shape surrounding it. Ketcham (1976) has implemented this approach through hardware and showed the effectiveness of local area histogram equalization (LAHE). Implementation of this method through software has been suggested by many authors, but it is far too inefficient for routine use since it requires that the pixel value distribution be determined anew for each pixel.

Figure 5-4. Contrast enhancement of human skull image by histogram equalization: (top) enhanced image, (bottom) corresponding histogram.

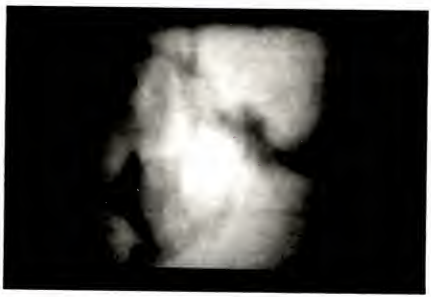

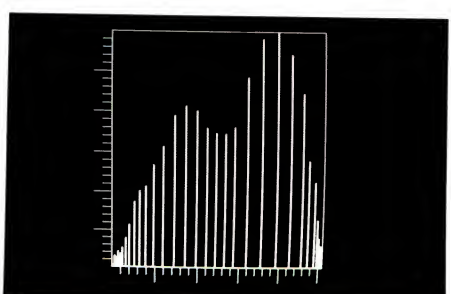

Pizer et al. (1984) described a simplified version of LAHE in which the desired gray level mapping is computed at a coarsely selected group of image points and the overall assignment scheme is completed by interpolation between the sample points. The regions associated with the sample points are termed basic contextual regions. The interpolation of the overall assignment schemes operates as follows (figure 5-5). At all pixels surrounded by four of these samples i.e., all but the image edge, interpolation is performed using the closest four basic contextual regions. In the case of the pixels at the corners, the assignment table from the closest region is used, where as for all other edge pixels interpolation is performed with the nearest two sample points. Thus, referring to the diagram in figure 5-5, let I(x) be the recorded intensity at a point x and g_s, g_t, g_u, and g_v are the gray level assignment functions corresponding to the basic contextual regions centered at s, t, u, and v, respectively. Then to compute the assigned gray level m(x) at a nonedge-or-corner pixel x, first g_s (I(x)) g_t(I(x)), g_u(I(x)), and g_v(I(x)) are determined and then interpolation is performed by the following bilinear interpolation formula

$$m(x)=a[bg_v(I(x))+(1-b)g_u(I(x))]$$

$$+[1-a][bg_t(I(x))+(1-b)g_s(I(x))] \qquad (5.16)$$

The choice of the size of a contextual region should depend upon the size of the features of an image to which

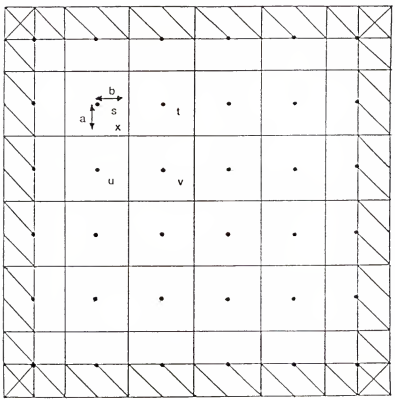

Subdivision and interpolation of a 6x6 pixel area. Open space-basic contextual region; ▨ -edge pixel; ⊠ -corner pixel; • -a sample point, center of a basic contextual region; X- a point at which a mapped intensity is to be computed.

Figure 5-5. Subdivision and interpolation of a 6 x 6 pixel area.

the method is applied. A region too large does not adapt well to local context, a region too small on the other hand emphasizes very local changes such as noise and edges but presents large structures poorly. A typical size of 64x64 works best for most clinical images and for small regions of interest a size of 32x32 is suitable. An example of enhancement of fluoro image of skull by AHE is shown in figure 5-6. Enhanced CAID images by AHE techniques are presented in Chapter IV.

Clipped adaptive histogram equalization

Although AHE produces good results, in certain cases noise becomes disturbingly obvious. In particular, this occurs where the image includes a poor SNR as in the case of fluoro images. The large noise enhancement is disturbing despite the fact that signal contrast is enhanced proportionately. A modification of this method, called clipped AHE also described by Pizer et al. (1986) avoids this overenhancement of noise. The concept of the clipped AHE can be understood by the following discussion.

Contrast enhancement can be defined as the slope of the function which maps input to output intensity. A slope of unity involves no enhancement, and higher slopes give increasingly higher enhancement. Thus, the limitation of contrast enhancement can be taken to involve restricting the slope of the mapping function.

Figure 5-6. Contrast enhancement of human skull image by AHE: (top) enhanced image, (bottom) corresponding histogram.

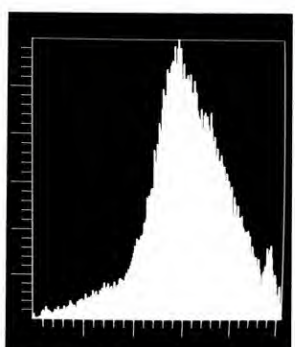

With histogram equalization the mapping function M(i) is proportional to the cumulative histogram

$$M(i) = \frac{(\text{Display-Range}) \times (\text{Cumulative Histogram}(i))}{\text{Region-Size}}.$$

Since the derivative of the cumulative histogram is the histogram, the slope of the mapping function at any input intensity, i.e., the contrast enhancement, is proportional to the height of the histogram at that intensity

$$\frac{dM(i)}{di} = \frac{(\text{Display-Range}) \times (\text{Histogram}(i))}{\text{Region-Size}}.$$

Therefore, limiting the slope of the mapping function is equivalent to clipping the height of the histogram.

High peaks in the histogram are normally caused by nearly uniform regions. In such a case, with the mapping due to ordinary histogram equalization a limited range of intensity values is mapped to a wide range of output intensity values, perhaps overenhancing the noise. But enforcing a maximum on the contents of the histogram bins limit the amount of contrast enhancement and thus the enhancement of noise.

When contrast enhancement is reduced at one location it must be increased in other areas so that the entire input intensity range will be mapped to the entire output intensity range. This corresponds to renormalizing the histogram after clipping so that its area returns to its

original value. This can be done by redistributing the clipped pixels uniformly among all histogram bins. Figure 5-7 illustrates the clipping of the original histogram. The effect of contrast enhancement on the skull image by clipped AHE is illustrated in figure 5-8.

Edge Enhancement

Sharpening techniques are used as enhancement tools for highlighting edges in an image. It is known that averaging pixels over a region tends to blur detail in an image. Since averaging is analogous to integration, it is natural to expect that differentiation will have the opposite effect and thus sharpen a given image.

The most commonly used method of differentiation in image processing applications is the gradient. Given a function f(x,y), the magnitude of the gradient of f at coordinates (x,y) is given by

$$G[f(x,y)]=[(df/dx)^2+(df/dy)^2]^{1/2}. \qquad (5.17)$$

For a digital image, the derivatives are approximated by differences. One such approximation is obtained by using absolute values, as given by

$$G[f(x,y)]= |f(x,y)-f(x+1,y)|+|f(x,y)-f(x,y+1)|. \qquad (5.18)$$

This formulation is suitable for computer implementation of the gradient operation. There are however, other variations of gradient operation.

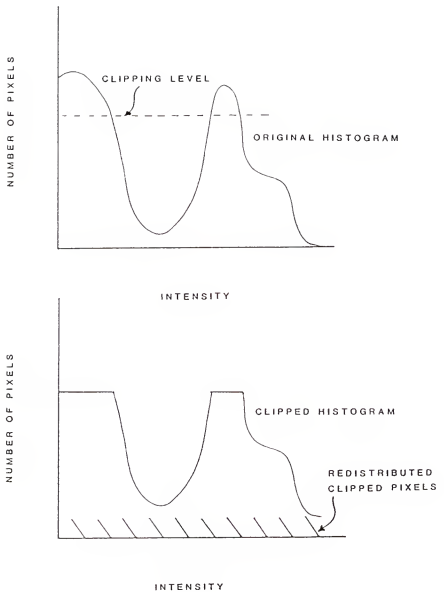

Figure 5-7. Clipping of the original histogram before applying AHE.

Figure 5-8. Contrast enhancement of human skull image by clipped AHE: (top) enhanced image, (bottom) corresponding histogram.

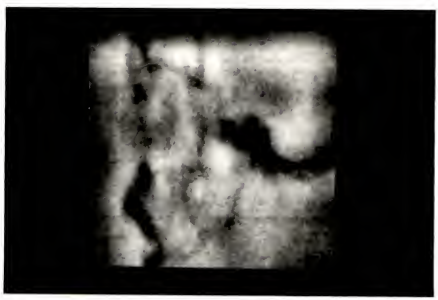

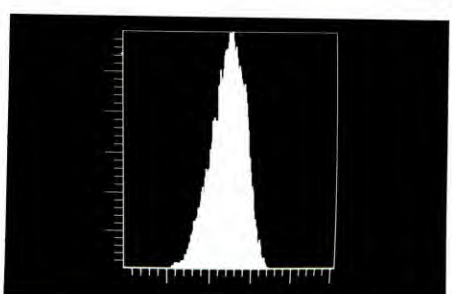

Once a method of approximating the gradient has been selected, there are numerous ways of using the results for generating a gradient image g(x,y). The simplest approach is to let the value of g at coordinates (x,y) be equal to the gradient of f at that point, that is,

$$g(x,y) = G[f(x,y)]. \tag{5.19}$$

The principal disadvantage of this method is that all smooth regions in f(x,y) appear dark in g(x,y). However, for the present application the following forms of gradient image were found useful

$$g(x,y) = \begin{cases} f(x,y) \pm E & \text{if } G[f(x,y)] \geq T \\ f(x,y) & \text{otherwise} \end{cases} \tag{5.20}$$

where T is some nonnegative threshold, and E is some positive value used to accentuate the desired edge. Computer programs were written with T and E as the variable parameters to generate gradient images.

The edge detection technique works well when the image contained low noise, as in the case of CAID produced images. Figures 4-23 and 4-24 show the effect of edge enahncement by gradient operation with a threshold value of ten.

Discussion

As a preprocessing technique the frame averaging of fluoroscopic images was found to be indispensible. Also, prior to enhancement smoothing by neighborhood averaging and median filtering was found to be very useful in reducing noise of images. Contrast enhancement by histogram equalization was found to be more useful than that achieved by a linear contrast stretching. Again, if enhancement in small detail throughout the image is desired the AHE and clipped AHE could be useful. Of course, as mentioned earlier the AHE works well if the image contains low noise. For most of the CAID images contrast scaling by linear transfer function with clipping as well as by AHE followed by edge enhancement yielded very good results.

To study the effectiveness of the image processing techniques on portal film images, the lateral image of a human cadaver head and AP view of a pelvis were digitized and processed. Figures 5-9 and 5-10 show the results. As can be seen, the enhanced images allow better visualization of the anatomical structures. A comparison between figures 5-9 and 4-24 show that enhanced CAID images are superior to the enhanced film images.

In conclusion, for the purpose of localization and verification of portal images, where radiation field edges and anatomical landmarks are the basic features of interest, a combination of smoothing, contrast enhancement by

Figure 5-9. Enhancement of a lateral view of the cadaver head film image: (top) original image, (upper left) enhancement by linear transfer function, (upper right) edge enhancement of the image of upper left, (lower left) enhancement by AHE, (lower right) edge enhancement of lower left.

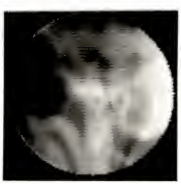

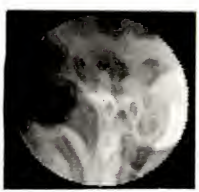

Figure 5-10. Enhancement of a pelvis port film image: (top) original, (bottom) enhancement by AHE.

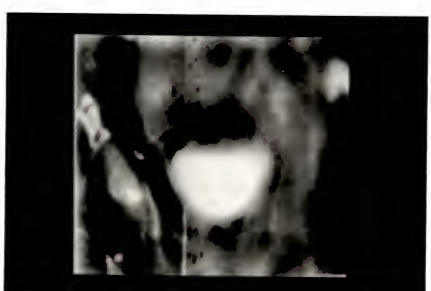

histogram modifications and edge detection can be useful image processing techniques.

CHAPTER VI
CONCLUSION

The goal of this project was to study the feasibility of a real-time digital imaging system for radiation therapy localization and verification. The performance of a prototype TV-fluoroscopic unit was studied. A prototype CAID was developed and its performance as a potential radiotherapy real-time imaging unit was evaluated.

The fluoro system has the advantage of being simple On terms of its components. The images produced by this system are comparable to conventional port film images. Because of its physical size however, the system can only be used for selected portals. Also, due to the low signal detection efficiency of the overall system, improvement of image quality by image processing is limited. However, a system with its various components optimized and used in combination with digital image processing may produce images with acceptable quality. The suitability of the fluoro system as a clinical radiotherapy imager requires further investigation.

The CAID, as a prototype imaging system, showed the most promise as a potential replacement for portal films. Phantom images obtained with the CAID were found to be superior to those obtained with the Fluoro system. This is

illustrated by figure 6-1, which compares the images of a pair of 9.0 cm long step wedges obtained by both the system. One of the step wedges has eight steps with a step size of 0.5 cm and is made of bone equivalent material. The other step wedge is made of solid water material and has eight steps with a step size of 1.0 cm. The steps are clearly visible in the CAID image but they are not visible in the fluoro image.

The images obtained by the CAID were found to have higher contrast than those of conventional port films; thus permitting better visualization of low contrast structures. In addition, digital image processing techniques provided an ability to optimize visualization of interesting anatomical structures which portal films do not provide. The further advantages offered by the CAID system as a real-time imager are many. The radiation portal could be monitored throughout the treatment. Verification of the proper setting of multileaf collimators for each treatment could be easily made. The reproducibility of patient positioning and effectiveness of immobilization devices could also be verified.

Several areas need further investigation before a clinically useful CAID system could be produced. The detecting medium for the prototype was iso-octane, a flammable liquid, which would pose a fire hazard in the event of leakage. Investigation may be needed to find an alternative detecting medium which would have high radiation detection

Figure 6-1. Images of a pair of step wedges: (top) fluoro image, (bottom) CAID image.

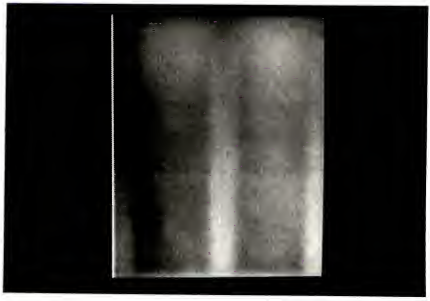

efficiency while presenting no physical hazard. Development of a practical device, having multiple strip detectors, is necessary to evaluate clinical performance of the CAID as a real-time imager.

To expedite the data collection for a practical CAID device, the measurements could be made with a continous rotation mode. In this mode however, consideration should be given to estimate an optimum rotational speed of the detector system. If the rotational speed is too high the arc length swept by each detector channel will be also long causing excessive averaging between pixels of assumed ray line and adjacent pixels. This could cause some kind of blurring in the reconstructed image. A suitable compromise would be to choose the speed so that the maximum arc length swept by the detector would not exceed the detector width. For example, if a 40 cm diameter field of view were to be imaged with detectors of 2 mm width; an arc of 0.57 degrees will be subtended by the central detector. If each measurement required 20 milliseconds then, according to the above criterion, 315 measurements could be made covering 180 degrees rotation in 6.3 seconds. However only about 160 angular increments are necessary for adequate reconstruction and thus sufficient time would be available, between measurements, for rotational movements and data storage necessary for the data acquisition sequence. Only further investigation can completely answer the questions about how much blurring will occur and what the minimum total

measurement time can be. Knowing the chamber response time and the relative contrast of test objects computer simulation could answer many of these questions prior to the instrument design phase.

As the prototype CAID was put together with ordinary unshielded cables imaging with this system in a high radio frequency field of a linear accelerator was not feasible. However, the principle of normalization with respect to a reference chamber seems to work to accomodate the pulsed nature of radiation. A system made with properly shielded cables and electronics should yield images with a linear accelerator of even higher contrast than the images with a cobalt source due to the smaller focal spot size.

APPENDIX A
RECONSTRUCTION ALGORITHM

Techniques of image reconstruction were first developed for use in radioastronomy by Bracewell (1956) for the purpose of identifying regions of the sun which emitted microwave radiation. Methods of reconstruction were also developed independently in electron microscopy (De Rosier and Klug 1968; Gordon, Bender, and Herman 1970) and in optics (Rowley 1969, Berry and Gibbs 1970). In the field of medical application, an x-ray computerized axial tomography (CAT) scanner was introduced in 1972 by EMI Ltd. (Hounsfield 1973). Reconstruction algorithms are discussed in detail by Gordon and Herman (1974) and by Brooks and Di Chiro (1976). A brief discussion of the methods which were of interest for the image reconstruction of the present work will be given below.

Definition of the Problem

The image reconstruction problem is, given a subset of all possible projections of an object, estimate its density distribution.

We suppose that there is a two-dimensional density distribution, $f(x,y)$ to be determined. Let an (x,y)

coordinate system be used to describe points in the density distribution. Let ray paths be described by an (r,s) coordinate system which is rotated by the same angle as the ray (figure A.1). Each ray is thus specified by the coordinates (r, ϕ), where ϕ is the angle of the ray with respect to the y-axis and r is its distance from the origin. The integral of the density function f(x,y) along a ray (r, ϕ) is called a ray-sum or ray-projection p and is given by

$$p(r, \phi) = \int_{r, \phi} f(x,y) ds. \qquad (A.1)$$

Ray sums at a particular angle are measured at n points, with regular intervals d across the diameter D [D=(n-1)d]. A complete set of ray sums at a given angle is called a projection or profile. Profiles are taken at equal angular increments from 0 to 180 degrees.

The role of the reconstruction algorithms is, to produce an estimate of the density distribution, f(x,y), using projection data as the input. Many mathematical approaches have been used for reconstruction, among these only the analytic methods of interest will be discussed.

Analytic Reconstruction

Analytic reconstruction is based upon the direct solution of equation (A.1). Implementation of these solutions requires that the density distribution be band limited, that is the

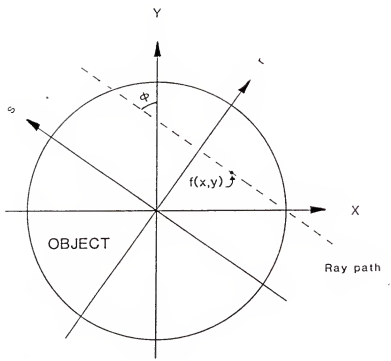

Figure A-1. Geometry of the image reconstruction problem.

object is assumed to contain no frequencies greater than a maximum frequency (K_m). This requirement of band limitation also limits the spatial resolution of the image. The assumption of band limitation has three major consequences: (1) the image may be reconstructed in an array of points with spacing $w=1/2K_m$, (2) the projections may be sampled at the same interval w, and (3) Fourier transforms may be replaced by discrete Fourier series.

While all analytic methods are theoretically equivalent, the various forms of their solution lead to significant differences in implementation. Two of the most important methods are discussed in the following.

Two-Dimensional Fourier Reconstruction

The density function f(x,y) can be represented in terms of the Fourier integral

$$f(x,y)=\int_{-\infty}^{\infty}\int_{-\infty}^{\infty}F(K_x,K_y)\exp[2\pi i(K_x x+K_y y)]dK_x dK_y. \quad (A.2)$$

Where $F(K_x,K_y)$ are the Fourier coefficients and K_x and K_y are the wave numbers in X and Y directions. $F(K_x,K_y)$ are given by the inverse Fourier transform:

$$F(K_x,K_y)=\int_{-\infty}^{\infty}\int_{-\infty}^{\infty}f(x,y)\exp[-2\pi i(K_x x+K_y y)]dxdy. \quad (A.3)$$

Equation (A.3) can be simplified if we rotate the (X,Y) axes to a new axes (r,s) as shown in figure(A-1), where the angle of rotation is given by

$$\phi = \tan^{-1}(K_y/K_x) \tag{A.4}$$

and by defining

$$K=(K^2_x+K^2_y)^{1/2}$$

one obtains,

$$F(K_x,K_y)=\int_{-\infty}^{\infty}\int_{-\infty}^{\infty} f(x,y)\ \exp(-2\pi iKr)\,dr\,ds. \tag{A.5}$$

By changing the order of integration, one can see that the s integral is just the ray-sum defined by equation (A.1), so that equation (A.5) becomes

$$F(K_x,K_y)=\int_{-\infty}^{\infty} p(r,\phi)\exp(-2\pi iKr)\,dr$$

$$=P(K,\phi) \tag{A.6}$$

where $P(K,\phi)$ is the Fourier transform of $p(r,\phi)$ with respect to r. Equation (A.6) states that each Fourier coefficient of the density function is equal to the corresponding Fourier coefficient of the projection taken at the same angle as the Fourier coefficient. This equation can be used for image reconstruction. Implementation of this equation requires taking the one-dimensional Fourier transform of each of the projections. Interpolation would provide a two-dimensional array of Fourier coefficients. Finally a two-dimensional inverse transform provides the desired image.

Bracewell (1956) derived this method of image reconstruction for his radioastronomy problem, however at that time computation of the two-dimensional Fourier

transform was prohibitive and he had to use an iterative method for actual reconstruction. Development of the Fast Fourier Transform and availability of high speed computers has changed the situation now. The method was also developed by DeRosier and Klug (1968) in electron microscopy and by Rowley (1969) in optical holography.

Filtered Back-projection

To understand the method of filtered back-projection a discussion of the concept of simple back-projection algorithm is essential. In the back-projection algorithm each profile is back-projected across the plane at the angle at which it was recorded, that is the magnitude of each ray sum is applied to all points that make up the ray. The process may be described by the following equation:

$$f(x,y) = \sum_{j=1}^{m} p(x\cos\phi_j + y\sin\phi_j, \phi)\,\Delta\phi \qquad (A.7)$$

where ϕ is the jth projection angle, m is the number of projections, $\Delta\phi$ is the angular increment between projections ($\Delta\phi = \pi/m$) and extends over all projections. Thus, the reconstructed density function f(x,y) is simply the sum of all ray sums passing through the point. For this reason back-projection is sometimes referred to as a summation method.

Back-projection does not produce a good reconstruction because each ray sum is applied not only to points of high

density, but all points along the ray. This causes a defect in the image which shows up most strikingly with discrete areas of high density producing a "star" artifact. If many projections are used, individual rays of the star may not be distinguishable, but there will be a general fogging of the background. Attempts have been made to compensate for this difficulty to a limited degree by looking for high density spots, calculating the corresponding patterns, and subtracting them from the image. However, reconstruction with filtered projection data yields better images as will be discussed in the following.

If we write the back-projection equation in integral form

$$f'(x,y)=\int_0^{\pi} p(x\cos\phi+y\sin\phi,\phi)\,d\phi \tag{A.8}$$

and replace $p(x\cos\phi+y\sin\phi,\phi)$ by its Fourier representation

$$p(r,\phi)=\int_{-\infty}^{\infty} P(K,\phi)\exp(2\pi iKr)\,dK \tag{A.9}$$

then we obtain

$$f'(x,y)=\int_0^{\pi}\int_{-\infty}^{\infty} P(K,\phi)\exp[(2\pi i\ K(x\cos\phi+y\sin\phi)]\,dK\,d\phi. \tag{A.10}$$

The integral can be put in a two-dimensional Fourier integral form in polar coordinates if the integrand is multiplied and divided by $|K|$. Thus taking the two-dimensional transform of equation (A.10) and using equation (A.6) one obtains

$$F'(K_x,K_y)=P(K,\phi)/|K| = F(K_x,K_y)/|K|. \qquad (A.11)$$

This equation implies that the back-projected image is equal to the true image except that its Fourier amplitudes are divided by the magnitude of the spatial frequency. Equation (A.11) suggests that the back-projection method can be made to work if the profiles are properly modified, or filtered, before being back-projected. Such an approach is called filtered back-projection. There are three variations of filtered back-projection, which will be discussed in the following.

Fourier filtering

The Fourier integral of density function f(x,y) in polar coordinates is given by

$$f(x,y)=\int_{-\infty}^{\infty}\int_{-\infty}^{\infty} F(K_x,K_y)\exp[2\pi iK(x\cos\phi+y\sin\phi)]|K|dKd\phi. \qquad (A.12)$$

Using equation (A.6) we get

$$f(x,y)=\int_0^{\pi} p'(r,\phi)d\phi \qquad (A.13)$$

where

$$p'(r,\phi)=\int_{-\infty}^{\infty} |K|P(K,\phi)\exp(2\pi iKr)dK. \qquad (A.14)$$

By inspection, one can see that equation (A.13) and (A.8) are identical, except that p' rather p is back-projected. The modification of p from p' is nothing but a filtering

operation, in which high frequency components are increased in proportion to their wave number. In practice equation (A.13) is implemented in terms of discrete summation,

$$f(x,y)=\sum_{j=1}^{m} p'(x\cos\phi_j+y\sin\phi_j,\phi_j)\,\Delta\phi. \qquad (A.15)$$

Radon filtering

Equation (A.14) represents the Fourier transform of the product of two functions $|K|$ and $P(K,\phi)$. The Fourier transform of $P(K,\phi)$ is $p(r,\phi)$, and Fourier transform, of K is $-1/2\pi^2r^2$ (Lighthill 1958). Applying the convolution theorem to equation (A.14) one obtains

$$p'(r,\phi)=-\frac{1}{2\pi^2}\int_{-\infty}^{\infty}\frac{p(r',\phi)\,dr'}{(r-r')^2}. \qquad (A.16)$$

Integration by parts yields

$$p'(r,\phi)=\frac{1}{2\pi^2}\int_{-\infty}^{\infty}\frac{\partial p(r',\phi)/\partial r'}{r-r'}. \qquad (A.17)$$

Equation (A.17) describes the filtering process as a single convolution integral in which the derivatives of p are added together, weighted by the inverse distance from the point at which the filtered value is desired. Equation (A.17) was first derived by Radon (1917) for solving gravitational equations. In recent years the method has been rediscovered several times and has been applied to x-ray imaging by Cormac (1973) and Beattie (1975).

Convolution filtering

By applying the convolution theorem (Bracewell 1965) equation (A.14) could be rewritten as

$$p'(r,)=\int_{-\infty}^{\infty} p(r',\phi)q(r-r')dr' \qquad (A.18)$$

where

$$q(r)=\int_{-\infty}^{\infty} |K| \exp(-2\pi iKr)dK. \qquad (A.19)$$

The integral of equation (A.19) cannot be evaluated as the integrand diverges. To overcome this difficulty one can replace the limit of integration $-\infty,+\infty$ by $-K_m,+K_m$ (Ramachandran and Laksminarayanan 1971). This replacement will not affect equation (A.14) because $P(K,\phi)$ is zero for $K>Km$, according to the assumption of band limitation. Thus, one needs to evaluate now

$$q(r)=\int_{-K_m}^{K_m} K\exp(-2\pi iKr)dK. \qquad (A.20)$$

Representing the radial distance in terms of the sampling interval $r=nw$, where $w=1/2K_m$, it can be shown that

$$\begin{aligned} q(nw)&=1/4w^2 && \text{for } n=0 \\ &=-1/\pi^2n^2w^2 && \text{for n odd} \\ &=0 && \text{for n even.} \end{aligned} \qquad (A.21)$$

Convolution operation with the kernel given by (A.20) is equivalent to a filter operation in frequency domain with a filter given by

$$Q(k) = |k| \qquad |k| \leq 1/2w$$
$$= 0 \qquad |k| > 1/2w \tag{A.22}$$

The geometrical representation of this filter resembles a ramp, hence the above method of back projection is termed as the ramp-filtered convolution back-projection method (CBPM). Now, if we have data for $p(r,\phi)$ at a set of equally spaced points $r=mw$,where m is a positive or negative integer, then equation (A.18) can be expressed in the form of an infinite sum as

$$p'(nw,\phi)=w \sum_{m=-\infty}^{\infty} p(mw,\phi)q[(m-n)w] \tag{A.23}$$

or, using equation (A.21)

$$p'(nw,\phi)=p(nw,\phi)/4w-(1/\pi^2w) \sum_{l-odd} p[(n+l)w,\phi]/l^2. \tag{A.24}$$

Shepp and Logan (1974) showed that at sharp boundaries the response of the CPBM is somewhat oscillatory. They proposed a modified convolution kernel given by

$$g'(nw)=-4/(\pi^2w\ (4n^2-1)) \qquad \text{for n integer} \tag{A.25}$$

and showed that reconstruction with this filter produces a damped oscillatory response. In an attempt to obtain a better reconstruction with noisy data they further modified the kernel, which is given by

$$g''(nw)= 0.4\ g'(nw) + 0.3\ g'(nw-w) + 0.3g'(nw+w). \tag{A.26}$$

Clearly the form of g''(nw) provides an averaging effect and thus helps reduce noise.

To reduce the oscillations at sharp boundaries Kwoh et al. (1977) proposed a parabolic filter function. The convolution kernel for this filter is given by

$$g'''(0) = \pi/3w^2$$
$$= -1/(\pi(nw)^2) \qquad \text{for n integer.} \qquad (A.27)$$

Comparison of Analytic Methods

The comparison between two-dimensional Fourier reconstruction and filtered back-projection is not simple. According to multiplication counts (Brooks and Dichiro 1976) the two-dimensional Fourier method may be faster, depending upon the details of implementation and image size. However, filtered back-projection has the advantage that each projection may be processed independently, as it is measured, so that reconstruction can proceed simultaneously with scanning. Both methods are faced with interpolation problems, but their nature is different. For the two-dimensional Fourier method, a two-dimensional interpolation in Fourier space is required, while with filtered back-projection, the values to be back-projected must be interpolated one-dimensionally.

The performance of filtered back-projection is not greatly affected by the choice of the filtering technique. The convolution technique is used because of its speed and

simplicity. Fourier filtering has the potential of being somewhat faster but its implementation is complicated.

Choice of the Reconstruction Method

Based on the selection criteria of the quality of the reconstructed image, computing time and data storage requirements the method of filtered back-projection was chosen for image reconstruction. Image reconstructions were performed with CBPM and Shepp-Logan filters. In the megavoltage imaging situations sharp boundaries are not usually encountered due to low differential absorption properties of patient anatomy. Thus, reconstruction by Shepp-Logan filter did not produce images of any better quality than that of ramp filter but did take more computing time. The noise reduction version of the Shepp-Logan filter however produces images of low noise when the data contained high statistical noise.

Theoretical and experimental experimental studies (Urie 1979) have shown that the CBPM works well for a similar type of coded-aperture device as is described in this investigation. This method offers good spatial resolution and handles noisy data satisfactorily. Also, according to Ramachandran and Laksminaryanan (1971) the covolution method seems to be better than the Fourier method from the viewpoint of speed and accuracy. Thus, the ramp-filtered CPBM was chosen for image reconstruction.

APPENDIX B
POINT SPREAD FUNCTION

The point spread-function (PSF) is defined as the radiation intensity distribution in the image of an infinitely small aperture (point source) radiating with unit intensity. It uniquely characterizes the transfer function of an imaging system. In a perfect imaging system the radiant energy emanating from a point source in the object plane would be concentrated at a point in the image plane; the ideal image point. In practical systems however, imperfections in the tranfer function result in a smearing or blurring of the energy around the ideal image point and therefore, an unsharp imaging of the point source results. The PSF provides a measure of this unsharpness.

Direct measurement of the PSF is difficult for two experimental reasons. First, in order to approximate a point source of radiation the aperture must be made quite small relative to the size of the point spread-function. Under practical conditions this allows a very low input radiation intensity into the system. Second, measurement of the resultant intensity distribution in the image plane requires scanning with a small aperture exactly through the center of the distribution which causes alignment difficulties. These experimental problems can be overcome

by measuring another transfer characteristic of the system, the edge response-function (ERF) from which the PSF can be calculated. As an intermediate step the line spread function (LSF) is calculated by differentiation of the ERF (Schneider and Bushong 1978).

Derivation of the PSF from the LSF

Formulation of the Problem

The relationship between LSF, I(x), and PSF, i(x,y), is given by

$$I(x)= \int_{-\infty}^{\infty} i(x,y)dy. \qquad (B.1)$$

The mathematical problem is thus, the LSF, I(x) is known, the function i(x,y) is to be deduced. Under the assumption of rotational symmetry of the PSF, the function i(x,y) can also be regarded as a function of x^2+y^2, i.e.,

$$I(x)=\int_{-\infty}^{\infty} f(x^2+y^2)dy. \qquad (B.2)$$

Solution of the Integral Equation

Equation (B.2) is the integral equation to be solved. By a change of variable the above equation can be rewritten as

$$I(x)= A(x^2)=A(t)=2\int_{0}^{\infty} f(t+y^2)dy, \quad t=x^2\geq 0 \qquad (B.3)$$

again, putting $u=t+y^2$

$$A(t)=\int_{t}^{\infty} f(u)(u-t)^{-1/2}du. \qquad (B.4)$$

Equation (B.4) is similar to the Abel equation. The solution of this equation can be obtained by a method described by Marchand (1964) and is given by

$$f(z)=\frac{2}{\pi}\frac{d}{dz}\int_0^\infty A(v^2+z)\,dv. \qquad (B.5)$$

Implementation of the Solution

Equation (B.5) was used to derive a graphical procedure, (Marchand 1964) to obtain the PSF from the LSF data. The procedure can be described in the following steps: (1) The function A(t) given by equation (B.3) was obtained by transferring each ordinate of the LSF curve to a new plot in which the abscissas represent the squares of the abscissas in LSF plot. (2) The next step was to generate a family of curves of $A(v^2+z)$ vs v with z as the parameter. (3) The area of each of the curves generated in step two was then determined and the magnitude of each area, suitably normalized, was then plotted against the corresponding value of z. The plot of these areas against z, of course represents,

$$\int_0^\infty A(v^2+z)\,dv.$$

(4) The slope of this curve was then determined for each value of z, and by equation (B.5), this slope represents f(z) except for the factor $2/\pi$. But z can be identified with x^2+y^2, which is the square of the distance from the

center of the desired point spread-function to the point in question. (5) Thus a plot of f(z) vs $z^{\frac{1}{2}}$ yielded the shape of the PSF.

Computer program was written to compute the PSF data from the LSF data.

REFERENCES

Albrecht, C., "Noise Sources in Image Intensifying Devices," In R. Moseley and J. Rust (Eds.), Diagnostic Radiologic Instrumentation, C. Thomas, Springfield, IL (1965).

Andrews, H. C., Tescher, A. G., and Krugar, R. P., "Image Processing by Digital Computer," IEEE Spectrum, 9(7): 20-32 (1972).

Baily, N. A., Horn, R. A., and Kamp, T. D., "Fluoroscopic Visualization of Megavoltage Therapeutic X-ray Beams," Int. J. Radiat. Oncol. Biol. Phys., 6(7): 935-939 (1980).

Barnes, G.T., and Brezovich, A., "The Design and Performance of a Scanning Multiple Slit Assembly," Med. Phys., 6(3): 197-204 (1979).

Beattie, J. W., "Tomographic Reconstruction from Fan Beam Geometry Using Radon's Integration Method," IEEE Trans. Nucl. Sci., NS-22: 1 (1975).

Berry, M. V., and Gibbs, D. F., "The Interpretation of Optical Projections," Proc. R. Soc. A., 314: 143-152 (1970).

Boag, J. W., "Ionization Chamber." In F. H. Attix and W. C. Roesch (Eds.), Radiation Dosemetry, Academic press, New York, NY (1966).

Bracewell, R. N., "Strip Integration in Radioastronomy," Austr. J. Phys., 9: 198-217 (1956).

Bracewell, R. N., The Fourier Transform and Its Applications, McGraw-Hill Book Company, New York, NY (1965).

Brooks, R. A., and Di Chiro, G., "Principle of Computed Assisted Tomography (CAT) in Radiographic and Radioisotopic Imaging," Phys. Med. Biol., 21(5): 689-732 (1976).

Byhardt, R. W., Cox, J. D., Hornburg, A., and Liermann, G., "Weekly Localization Films and Detection of Field Placement Errors," Int. J. Radiat. Oncol. Biol. Phys., 4: 881-887 (1978).

Chu, A., and Fletcher, G. H., "Incidence and Causes of Failures to Control by Irradiation the Primary Lesions in Squamous Cell Carcinomas of the Anterior Two-Thirds of the Toungue and Floor of Mouth," Am. J. Roentgenol. Radium Ther. Nucl. Med., 117: 502-508 (1973).

Chu, J. C. H., Grant, W. H., and Almond, P. R., "A Liquid Ionization Chamber for Neutron Dosimetry," Phys. Med. Biol., 25(6): 1133-1148 (1980).

Cormac, A. M., "Reconstruction of Densities from their Projections, with Applications in Radiological Physics," Phys. Med. Biol., 18: 195-207 (1973).

Csorba, I. P., Image Tubes, Howard W. Sams & Co., Inc., Indianapolis, IN (1985).

Curry, T. S., Dowdey, J. E., and Muray, R. C., Christensen's Introduction to the Physics of Diagnostic Radiology, Lea and Febiger, Philadelphia, PA (1984).

DeRosier, D., and Klug, A., "Reconstruction of Three Dimensional Structures from Electron Micrographs," Nature, 217: 130-134 (1968).

Droege, R. T., and Bjarngard, B. E., "Metal Screen Film Detector MTF at Megavoltage x-ray Energies," Med. Phys., 6: 515-518 (1979a).

Droege, R. T., and Bjarngard, B. E., "Influence of Metal Screens on Contrast in Megavoltage x-ray Imaging," Med. Phys., 6: 487-493 (1979b).

Fitzgerald, L. T., "A Repetitive Integral Measurement Technique for X and Gamma Radiation Dosimetry and Depth Dose Scanning," Doctoral Dissertation, University of Florida (1974).

Glinas, M., and Fletcher, G. H., "Incidence and Causes of Local Failure of Irradiation in Squamous Cell Carcinoma of the Faucial Arch, Tonsillar Fossa and Base of the Tongue," Radiology, 108: 383-387 (1973).

Gonzalez, R. C., and Wintz, P., Digital Image Processing, Addison-Wesley Publishing Company, Reading, MA (1977).

Gordon, R., and Herman, G. T., "Three-Dimensional Reconstruction from Projections: A Review of Algorithms," Int. Rev. Cytol., 38: 111-151 (1974).

Gordon, R., Bender, R., and Herman, G. "Algebraic Reconstruction Techniques (ART) for Three Dimensional Electron Microscopy and X-ray Photography," J. Theor. Biol., 29: 471-481 (1970).

Hall, E. L., "Almost Unifiform Distribution for Computer Image Enhancement," IEEE Trans. Computers, C-23(2): 207-208 (1974).

Hammoudah, M. M., and Henschke, U. K., "Supervoltage Beam Films," Int. J. Radiat. Oncol. Biol. Phys., 2: 571-577 (1977).

Haque, P., and Stanley, J. H., "Basic Principles of Computed Tomography Detectors." In T. H. Newton and D. G. Potts (Eds.), Radiology of the Skull and Brain; Technical Aspects of Computed Tomography, The C. V. Mosby Company, St. Louis (1981).

Haus, A. G., and Marks, J. E., "Detection and Evaluation of Localization Errors in Patient Radiation Therapy," Investigative Radiology, 8(6): 384-391 (1973).

Hounsfield, G. N., "Computerized Transverse Axial Scanning (Tomography) Part 1, Discussion of System," Br. J. of Radiology, 46: 1016-1022 (1973).

Johansson, K. A., and Svensson, H., "Liquid Ionization Chamber for Absorbed Dose Determinations in Photon and Electron Beams," Acta Radiol. Oncol., 21: 359-367 (1982).

Johns, H. E., and Cunningham, J. R., The Physics of Radiology, C. Thomas, Springfield, IL (1983).

Joseph, P. M., "Artifacts in Computed Tomography," Radiology of the Skull and Brain, Technical Aspects of Computed Tomography, The C. V. Mosby Company, St. Louis (1981).

Ketcham, D. J., "Real-Time Image Enhancement Techniques," Proceedings SPIE/OSA Conference on Image Processing, 74, 120-125 (1976).

Kwoh, Y., Reed, I., and Truong T., "A Generalized $|w|$-Filter for 3-D Reconstruction," IEEE Trans. Nucl. Sci., NS-24: 1990-1998 (1977).

Lam, K. S., Partomah, M., and Lam, W. C., "An On-Line Electronic Portal Imaging System for External Beam Radiotherapy," Br. J. of Radiology, 59: 1007-1013 (1986).

Leong, J., "A Digital Image Processing System for High Energy x-Ray Portal Images," Phys. Med. Biol., 29: 1527-1535 (1984).

Leong, J., "Use of Digital Fluoroscopy as an On-Line Verification Device in Radiation Therapy," Phys. Med. Biol., 31(9): 985-992 (1986).

Lighthill, M. J., Introduction to Fourier Analysis and Generalized Functions, Cambridge University Press, London (1958).

Lim, C. B., Han, K. S., Hawman, E. G., and Jaszczak R. J., "Image Noise, Resolution, and Lesion Detectibility in Single Photon Emission CT," IEEE Trans. Nucl. Sci., Ns-29: 500-505 (1982).

Luthmann, R., "Rotational Parallel Plate Radionuclide Imaging Device," Doctoral Dissertation, University of Florida (1978).

Marchand, E. W., "Derivation of The Point Spread Function from the Line Spread Function," Journal of the Optical Society of America, 54(7): 915-919 (1964).

Marks, J. E., Haus, A. G., Sutton, H. G., and Griem, M. L., "Localization Error in the Radiotherapy of Hodgkin's Disease and Malignant Lymphoma with Extended Mantle Field," Cancer, 34: 83-90 (1978).

Mauderli, W., and Fitzgerald, L. T., "Rotating Laminar Emission Camera(ROLEC) with Ge-Detector: Further Developments," Med. Phys. (in press).

Mauderli, W., Fitzgerald, L. T., Urie, M. M., and Toswill C.H., "Rotating Laminar Emission Camera with GE-Detector: An Analysis, " Med. Phys., 8(6): 871-876 (1981).

Mauderli, W., Luthman, R. W., Fitzgerald, L.T., Urie, M. M., Williams, C. M., Toswill, C. H., and Entine, G., "A Computerized Rotating Laminar Radionuclide Camera," Journal of Nuclear Medicine, 20(4): 341-344 (1979).

Meertens, H., "Digital Processing of High Energy Photon Beam Images," Med. Phys., 12: 111-113 (1985).

Meertens, H., van Herk, M., and Weeda, J., "A Liquid Ionization Detector for Digital Radiography of Therapeutic Megavoltage Photon Beams," Phys. Med. Biol., 30(4): 313-321 (1985).

Nelson, R. S., Barbaric, Z. L., Gomes, A. S., Moler, C. L., and Deckard, M. E., "An Evaluation of Fluoroscent Screen-Isocon Camera System for X-Ray Imaging in Radiology," Med. Phys., 9(5): 777-783 (1982).

Papoulis, A., Probability, Random Variables and Stochastic Processes, McGraw-Hill, New York, NY (1965).

Peschmann, K. R., "Xenon Gas Ionization Detectors," In T. H. Newton and D. G. Potts (Eds.), Radiology of the Skull and Brain; Technical aspects of Computed Tomography, The C. V. Mosby Company, St. Louis (1981).

Pizer, S. M., Austin, J. D., Perry, J. R., and Safrit, H. D., "Adaptive Histogram Equalization for Automatic Contrast Enhancement of Medical Images," Technical Report 86-010, University of North Carolina at Chapel Hill (1986).

Pizer, S. M., Zimmerman, J. B., and Staab, E. V., "Adaptive Grey Level Assignment in CT Scan Display," Journal of Computer Assisted Tomography, 8(2): 300-305 (1984).

Pratt, W. K., Digital Image Processing, John Wiley & Sons, New York, NY (1978).

Radon, J., "On the Determination of Functions from Their Integrals Along Certain Manifolds," Ber. Saechs. Akad. Wiss. Lepzig, Math-Phys. Kl., 69: 262-277 (1917).

Ramachandran, G. N., and Laksminaryanan, A. V., "Three Dimensional Reconstruction from Radiographs and Electron Micrographs: Application of Convolutions Instead of Fourier Transforms," Proc. Natl. Acad. Sci. U. S. A., 65: 2236-2240 (1971).

Reinstein, L. E., Alquist, L., Amols, H. I., and Lagueux, B., "Quantitative Evaluation of a Portal Film Contrast Enhancement Technique," Med. Phys., 14(3): 309-313 (1987).

Reinstein, L. E., Durham, M., Tefft, M., Yu, A., and Glicksman, A. S., "Portal Film Quality: A Multiple Institutional Study," Med. Phys., 11: 555-557 (1984).

Reinstein, L.E., and Orton, C. G., "Contrast Enhancement of High Energy Radiotherapy Films," Br. J. of Radiology. 52: 880-887 (1979).

Rowley, P. D., "Quantitative Interpretation of Three-Dimensional Weakly Refractive Phase Objects Using Holographic Interferometry," J. Opt. Soc. Am., 59: 1496-1498 (1969).

Schneider, N. J., and Bushong, S. C., "Single Step Calculation of the MTF from ERF," Med. Phys., 5: 31-33, (1978).

Shalev, S., and Arenson, J., "Digital Enhancement of Treatment Verification Films," Radiology, 153(P): 154,(1984).

Shepp, L. A., and Logan, B. F., "The Fourier Reconstruction of a Head Section," IEEE Trans. Nucl. Sci., NS-21: 21-43, (1974).

Tabrosky, S. C., Lam, W. C., Sterner, R. E., and Skarda, G. M., "Digital Imaging for Radiation Therapy Verification," Optical Engineering, 21(5): 888-893 (1982).

Tanaka, E., and Iinuma, T. A., "Correction Functions for Optimizing the Reconstructed Image in Transverse Section scan," Phys. Med. Biol., 20(5): 789-798 (1975).

Urie, M. M., "The Rotating Laminar Emission Camera: An Investigation of Its Potential as a Clinical Device for Imaging in Two Dimensions Three Dimensional Distributions of Radioactivity," Doctoral Dissertation, University of Florida (1979).

Urie, M. M., Mauderli, W., Fitzgerald, L. T., Williams, C. M., and Tosswill, C. H., "Rotating Laminar Emission Camera with GE-Detector: Experimental Results," Med. Phys., 8(6): 865-870 (1981).

Wickman, G., "A Liquid Ionization Chamber with High Spatial Resolution," Phys. Med. Biol., 19(1): 66-72 (1974).

Wilenzick, R. M., Merritt, C. R. B., and Balter, S., "Megavoltage Portal Films Using Computed Radiographic Imaging with Photostimulable Phosphors," Med. Phys., 14(3): 389-392 (1987).

BIOGRAPHICAL SKETCH

Mohammad Khairul Islam was born on April 1, 1953, in Bogra, Bangladesh. He attended primary and secondary schools of Bogra and received his degree in Secondary School Certificate in 1968. He then attended Dinajpur College and received his Higher Secondary Certificate degree in 1970.

He entered the University of Rajshahi, in Bangladesh, in 1970 to attend the honors program in physics. Due to the liberation war of Bangladesh in 1971 his education was interrupted like everyone else's in that country. Subsequently he received his Bachelor of Science degree with honors in physics in 1975, and Master of Science in physics in 1977 from the University of Rajshahi.

After receiving his master's degree he accepted the position of a research officer at the Bangladesh Council of Scientific and Industrial Research, where he was engaged in the study of utilization of solar energy.

In 1980, he started his graduate work at the University of Florida and received his master's degree in physics in 1983. In January, 1984 he entered the medical physics program in the department of Nuclear Engineering Sciences, at the University of Florida. Since then he has held a graduate assistantship in the department of Radiation Therapy.

I certify that I have read this study and that in my opinion it conforms to acceptable standards of scholarly presentation and is fully adequate, in scope and quality, as a dissertation for the degree of Doctor of Philosophy.

Francis J. Bova, Chairman
Assistant Professor of
Nuclear Engineering Sciences

I certify that I have read this study and that in my opinion it conforms to acceptable standards of scholarly presentation and is fully adequate, in scope and quality, as a dissertation for the degree of Doctor of Philosophy.

Lawrence T. Fitzgerald, Co-Chairman
Associate Professor of Nuclear
Engineering Sciences

I certify that I have read this study and that in my opinion it conforms to acceptable standards of scholarly presentation and is fully adequate, in scope and quality, as a dissertation for the degree of Doctor of Philosophy.

Walter Mauderli
Professor of Nuclear Engineering
Sciences

I certify that I have read this study and that in my opinion it conforms to acceptable standards of scholarly presentation and is fully adequate, in scope and quality, as a dissertation for the degree of Doctor of Philosophy.

Genevieve Roessler
Associate Professor of
Nuclear Engineering Sciences

I certify that I have read this study and that in my opinion it conforms to acceptable standards of scholarly presentation and is fully adequate, in scope and quality, as a dissertation for the degree of Doctor of Philosophy.

Rodney R. Million
Professor of Radiation Therapy

I certify that I have read this study and that in my opinion it conforms to acceptable standards of scholarly presentation and is fully adequate, in scope and quality, as a dissertation for the degree of Doctor of Philosophy.

Joseph N. Wilson
Assistant Professor of Computer
and Information Sciences

This dissertation was submitted to the Graduate Faculty of the College of Engineering and to the Graduate School, and was accepted as partial fulfillment of the requirements for the degree of Doctor of Philosophy.

December 1987

Hubert A. Bevis
Dean, College of Engineering

Dean, Graduate School